Dielectric Permittivity Measurements of Electronics Cooling Fluids

by

Alexander Helmut Pfeiffenberger

A thesis submitted to the Graduate Faculty of
Auburn University
in partial fulfillment of the
requirements for the Degree of
Master of Science

Auburn, Alabama
December 14, 2013

Keywords: Dielectric Fluids, Microstrip, Ring Resonator, Characterization, HFSS

Approved by

Michael C. Hamilton, Chair, Assistant Professor of Electrical and Computer Engineering
Stuart Wentworth, Associate Professor of Electrical and Computer Engineering
Virginia A. Davis, Sanders Associate Professor of Chemical Engineering
John Evans, Technology Management Professor of Industrial and Systems Engineering

Abstract

High performance electronics often present heat management challenges which can, in some applications, be mitigated through the use of liquid cooling technologies. In this work, select 3M™ Novec™ and 3M™ Fluorinert™ dielectric fluids are investigated using open-ended coaxial probe, microstrip ring resonator, and microstrip transmission line measurements. Microstrip structures in air are used to extract the relative permittivity of these fluids from the measured effective permittivity. Microstrip structures in 3M™ fluids are simulated using the electromagnetic finite element solver ANSYS HFSS to match measured effective permittivity. An approximation of the frequency dependent relative permittivities and loss tangents are provided up to 50GHz for 3M Novec-649™, Novec HFE-7100™, and Fluorinert FC-72™. The feasibility of using ring resonator structures to detect specific contaminants within these dielectric fluids is also explored.

Acknowledgments

The author would like to express his appreciation to Dr. Michael C. Hamilton for serving as his advisor and providing significant assistance throughout this work and his graduate studies. Dr. Virginia A. Davis, Dr. Stuart Wentworth, and Dr. John Evans are also thanked for their review and commentary.

The author would also like to thank George A. Hernandez, John P. Bailey III, Jorge S. Hurtarte, and Christopher K. Clayton for their assistance in many aspects of this work.

A personal note of appreciation goes to Brigitte, Helmut, and Philipp Pfeiffenberger for their support throughout the author's academic endeavors.

Table of Contents

List of Tables

List of Figures

Chapter 1

Introduction

Liquid cooling systems provide a means of maintaining a controlled operating environment in applications where the power density of the electronic load cannot be mitigated by means of traditional forced air cooling. These systems may comprise high speed and high performance digital, mixed-signal or other RF and microwave components with high dissipated power densities, which can lead to challenging thermal environments. When direct immersion in pool or circulated dielectric fluids is required (to ensure device temperatures remain within specification) it is advantageous to use an inert and insulating (dielectric) fluid. To facilitate system level integration, accurate component design and understanding of the impact on system performance of the dielectric response of these fluids on exposed packaging and integration components such as connectors and printed circuit board launches and transitions must be characterized with consideration of the broadband complex permittivity of these fluids.

Two fundamental parameters used to characterize dielectric materials are known colloquially as the dielectric constant and loss tangent [1]. These parameters determine the formation of electric fields when charge is present across an insulating material, and how energy is dissipated within the material. Given an electric field across a material, the material can become polarized, and the degree to which a material is susceptible to polarization is termed the electric susceptibility, given in Equation 1.5 [2]. The term dielectric constant is a misnomer, as both the real and imaginary components of the complex permittivity (Equation 1.2) may exhibit frequency dependence. In this work, the term relative permittivity (Equation 1.3) is

used to refer to the magnitude of the real component of the complex permittivity relative to the permittivity of free space, which is given in Equation 1.1 [2]. The relative permittivity is related to energy storage, [3] [4] while the ratio of the relative imaginary component (Equation 1.4) to the relative real component (Equation 1.3) is called the loss tangent (Equation 1.6), where the imaginary component accounts for loss of energy to the material.

$$\epsilon_0 = 8.854 \times 10^{-12} F/m \tag{1.1}$$

$$\epsilon^*(\omega) = \epsilon'(\omega) + j\epsilon''(\omega) \tag{1.2}$$

$$\epsilon'_r(\omega) = \epsilon'(\omega)/\epsilon_0 \tag{1.3}$$

$$\epsilon''_r(\omega) = \epsilon''(\omega)/\epsilon_0 \tag{1.4}$$

$$\chi_e(\omega) = \epsilon'_r(\omega) - 1 \tag{1.5}$$

$$tan\delta(\omega) = \epsilon''_r(\omega)/\epsilon'_r(\omega) \tag{1.6}$$

Manufacturers of materials used in microwave applications often only provide the relative permittivty and loss tangent over a narrow frequency range, leaving the system designer to assume that these values do not vary sigificantly with frequency. In the case of the dielectric liquids of interest (hereafter referred to as Novec-649, HFE-7100 and FC-72), the relative permittivity and dielectric strength have been provided via datasheets from the manufacturer [5] [6] [7].

Fluid	**Relative Permittivity (ϵ_r')**	**Dielectric Stength (kV) 0.1" gap**
FC-72	1.75 (1kHz)	>40
HFE-7100	7.39 (100Hz-10MHz)	∼40
Novec-649	1.8 (1kHz)	>40

Table 1.1: Manufacturer provided relative permittivity and dielectric strength.

Although engineered fluids such as those listed in Table 1.1 are chemically and thermally stable, exposure to moisture, plasticizers extracted from components, or other direct contamination may impact the electrical and thermal properties of the fluid. As dielectrics have bound charges that influence the field within the material [2], the complex permittivity of a cooling fluid can be correlated to the presence of certain contaminates or changes in the molecular structure fluid. Such studies can be done by establishing a precise measurement and noting perturbation, or through the establishment of a precise and accurate measurement technique that can be used to extract the complex permittivity of a contaminated fluid.

In this thesis we assess the usefulness of an open-ended coaxial probe and microstrip ring resonator in establishing a baseline measurement of the complex permittivity of each dielectric fluids given in Table 1.1. Additionally, testing at DC of both pristine and perturb fluids is performed. The complex permittivities of perturbed fluids are also measured using both the open-ended coaxial probe and microstrip ring resonator. It was found that HFE-7100 is well suited for measurement via open-ended coaxial probe, while FC-72 and Novec-649 can be more accurately and precisely measured using a microstrip ring resonator. Measurements made using microstrip structures will give an effective relative permittivity (as described in section 2.3.2), from which a relative permittivty can be extracted through simulation using the electromagnetic finite element solver ANSYS high frequency structural simulator (HFSS). Improvements to the technique used to extract the complex permittivity of a dielectric fluid using microstrip ring resonators are discussed as future work.

Chapter 2

Background

In this chapter we describe the means by which the dielectric properties described in the previous chapter can be measured. While it is possible to construct a parallel plate capacitor using the dielectric fluid of interest and measure the impedance of this system; coaxial probe, transmission line, resonant cavity, and free space techniques are more commonly used for frequencies above 1GHz. [4]. Numerous factors determine which measurement technique should be used, including frequency range and the values of ϵ_r and tanδ. In this work a commercial open coaxial probe is first used to measure all three fluids of interest. As will be shown, air, Novec-649, and FC-72, each with a low dielectric constant and loss are better suited to measurement with the ring resonator technique than to measurement using a coaxial probe. In the case of the coaxial probe, the extraction is done using software designed by Agilent Technologies. Where the commercial probe is unable to produce accurate measurement results, a combination of microstrip transmission line, microstrip ring resonator, and ANSYS HFSS simulation is used to establish the permittivity and loss tangent of the two low loss fluids; Novec-649 and FC-72. A simplified flow chart for this technique is shown in Figure 2.1, illustrating the order in which measurement and fitting through simulation was performed.

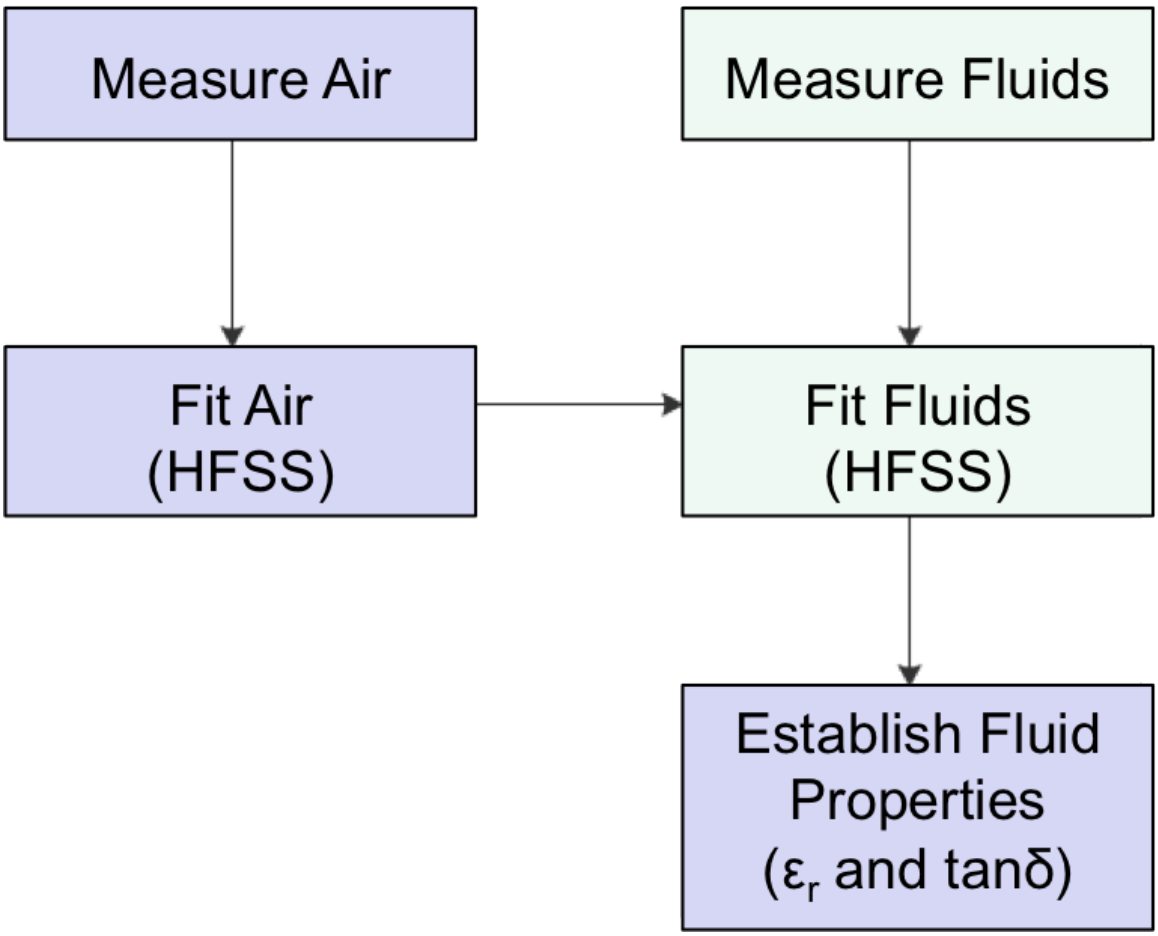

Figure 2.1: This flow chart illustrates that measurement and simulation of the ring resonator in air must be performed to establish the substrate permittivity before measurement and simulation of the ring resonator in a dielectric fluid can be used to establish the permittivity of the fluid itself.

Each measurement performed in this work, with the exception of DC analysis, relies on a signal generated by a vector network analyzer (VNA), which is transmitted such that the material of interest absorbs energy across a wide range of swept frequencies. The accuracy provided by a VNA in measuring the complex ratio of the reflected signal to the incident signal (S_{11} or return loss) as well as the ratio of the transmitted signal to the incident signal (S_{21} or insertion loss) is extended right up to the device under test (DUT) using calibration, as discussed in Appendix B. Data from measurements and simulations are stored and processed as scattering matrices, which provide a complete description of the network as seen at its ports. [8] In the case of the two-port network used in this work, the matrix is comprised of four terms; describing power being reflected back from each port and power flowing between ports.

2.1 DC Bias

The structure shown in Figure 2.2 is comprised of a metalization on an insulating substrate. Wire leads are soldered to each pad and connected to a Keithley Model 248 High Voltage Supply. This supply can produce a maximum output voltage of 5kV, which will be present across the 0.5mm gap between both pads.

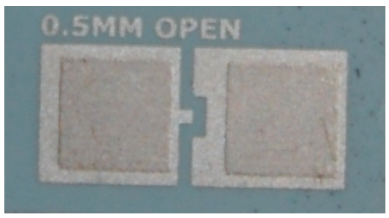

Figure 2.2: A structure comprised of metalization and a gap of fixed width was used for DC bias testing.

The combination of gap width and applied voltage creates a field of 10kV/mm, which is below the field strength required for dielectric breakdown as given (in terms of kV across a 2.54mm gap) for each dielectric fluid in Table 1.1. Therefore, it was

expected and confirmed that current did not flow when the gap structure was placed into a dielectric fluid while under bias.

2.2 Open-Ended Coaxial Probe

The open-ended coaxial probe designed by Agilent Technologies is shown in Figure 2.3 and makes use of a one-port measurement and proprietary software to provide end-users with a means of measuring the complex permittivity of fluids and other soft materials into which the probe can be inserted.

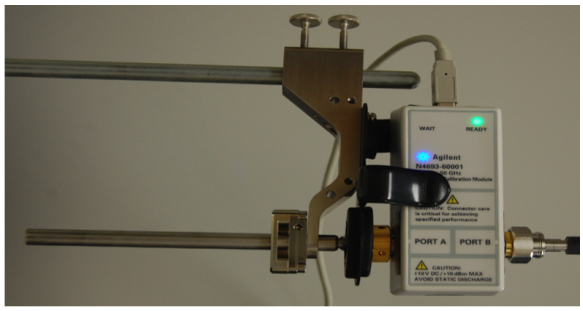

Figure 2.3: Agilent 85070E performance probe mounted on a stand and connected to an electronic calibration unit (Agilent N4693A).

For this measurement a signal generated by the VNA travels through the probe body and out of the probe tip. The escaping signal will be partially absorbed by the dielectric fluid and partially reflected back to the probe. The proprietary software provided by Agilent Technologies uses this ratio across frequency to provide the end-user with both $\epsilon_r'(\omega)$ and $\epsilon_r''(\omega)$ which comprise the complex relative permittivity. As is described in Section 3.2, the performance probe cannot be used to characterize the complex permittivity of low-loss fluids such as Novec-649 or FC-72. However, the open-coaxial probe can provide an accurate measurement of HFE-7100 and served as a useful tool in the study of perturbed fluids, as shown in Chapter 4.

2.3 Transmission Lines

In basic circuit theory the electric wavelengths passing through a network are assumed to be much larger than the network elements themselves. However, in the case of transmission lines, the circuit elements may be a fraction of a wavelength or many wavelengths in size. This makes transmission lines distributed-parameter networks, where voltages and currents can vary in magnitude and phase across the structure. Transmission line theory aims to bridge the more complex field analysis and basic circuit theory. [8] Two of the most common transmission line types found in microelectronics are stripline and microstrip.

2.3.1 Stripline

Stripline is a planar type of transmission line. The geometry is shown in Figure 2.4 and consists of a thin conducting strip with specific height (t) and width (W) centered between two conducting ground planes spaced apart by a specific distance (d). In this simplified representation the dielectric is illustrated in green and the metalization is shown in yellow.

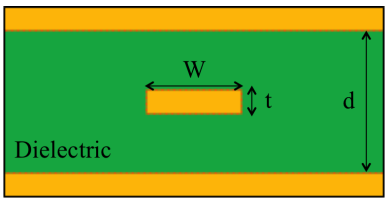

Figure 2.4: Schematic cross section of stripline.

The combination of dielectric properties, metal conductivity, and geometry results in a specific characteristic impedance. The characteristic impedance is a ratio of the amplitudes of voltage and current of a single wave propagating along the line. [8] To match the port impedence between various structures and test equiptment most

transmission lines are designed to have a characteristic impedance of 50Ω.

Because the signal conductor resides within a dielectric it can be difficult to connect stripline to components such as transistors or capacitors. [2] However, having two conductors and a homogenous dielectric, allows stripline to support a transverse electromagnetic (TEM) wave. A TEM wave is characterized by a lack of longitudinal field components, meaning the transverse fields are the same as the static fields existing between conductors.

Another important characteristic of a transmission lines that should be considered in addition to the characteristic impedance is the phase velocity, which describes the rate at which the phase of the signal propagates along the structure. The phase velocity (v_p), of the TEM propagation mode is given in equation 2.1 [8]. Higher order modes can propagate as well, but can often be eliminated using shorting or pinning vias between the ground planes. [8]

$$v_p = \frac{c}{\sqrt{\epsilon_r}} \tag{2.1}$$

2.3.2 Microstrip

Microstrip is another type of planar transmission line. The geometry is shown in Figure 2.5 and consists of a thin conducting strip with specific height (t) and width (W) above a dielectric and single conducting ground plane. A specific distance (d) is maintained between the conducting strip and the ground plane. In this simplified representation the dielectric is illustrated in green and the metalization is shown in yellow.

Because the signal conductor is exposed, it is more straightforward to connect components such as transistors or capacitors to microstrip transmission lines than it

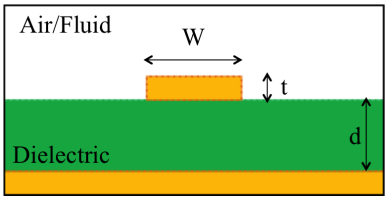

Figure 2.5: Schematic cross section of microstrip.

is to connect them to stripline. Additionally, the fabrication of a microstrip transmission line simply requires one side of a metal-clad dielectric to be masked and etched. However, as the dielectric substrate does not fill the region above the conducting strip the behavior and analysis of a microstrip transmission line is made somewhat more complex than that of the stripline. This inhomogeneous dielectric means that the microstrip cannot support a pure TEM wave as the phase velocity within each dielectric (substrate and fluid or air) will be different. [8] In most practical applications the fields can be considered as quasi-TEM. [2] Just as with the stripline, the characteristic impedance of the microstrip can be manipulated by altering the geometry or conductor and dielectric material properties.

The concept of an effective dielectric permittivity allows the pair of dielectric materials to be interpreted as a homogenous material. One such semi-empirical interpretation for a microstirp in air is given in Equation 2.2. [8] When we assume TEM propagation for simplicity we find that the propagation velocity (v_p) is related to the speed of light (c) by Equation 2.3, which when divided by a particular frequency, provides the physical length of one wavelength at the frequency along the transmission line. This is called the guide wavelength (Equation 2.4). [2]

$$\epsilon_{eff} = \frac{\epsilon_r + 1}{2} + \frac{\epsilon_r - 1}{2} \frac{1}{\sqrt{1 + 12d/W}} \tag{2.2}$$

$$v_p = \frac{c}{\sqrt{\epsilon_{eff}}} \tag{2.3}$$

$$\lambda_g = \frac{v_p}{f} \tag{2.4}$$

Transmission lines can be used for more than simple point-to-point connections, as explored in the next section where transmission lines are used to construct high-Q resonating structures.

2.4 Ring Resonators

A ring resonator is primarily comprised of a transmission line forming a closed loop and can be implemented using microstrip or stripline transmission lines.

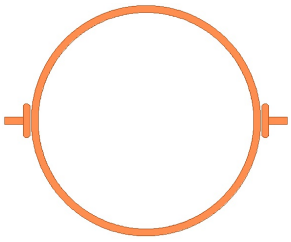

Figure 2.6: Top view of a ring resonator showing feed lines, coupling structures, and the ring itself.

Ring resonators can be used for accurate and precise measurements of dielectric materials. As voltages and currents vary in magnitude and phase over the structure, it is possible to find a material's permittivity based on known relationships between geometry, material properties, and frequency. These relationships are reflected in the location and bandwidth of the resonant peaks and will outlined in this section. Details on the specific implementation of the ring resonator used in this work are found in Section 3.3.2.

The quality factor (Q) of a resonant structure is a measure of the damping present in the system, with a higher value of Q indicating lower loss. [8]

$$Q = \omega \frac{\text{average energy stored}}{\text{energy loss / second}} \tag{2.5}$$

In the case of the microstrip transmission line based ring resonator used in this work, loss can be attributed to the dielectric (α_d), the conductor (α_r), and to radiation (α_r) as shown in Equations 2.9 and 2.10. The resonator should be loosely coupled to the feed-lines to maintain a high Q. [8] Coupling between feed-lines and the ring structure can be achieved across an air gap as is shown in Figure 2.7.

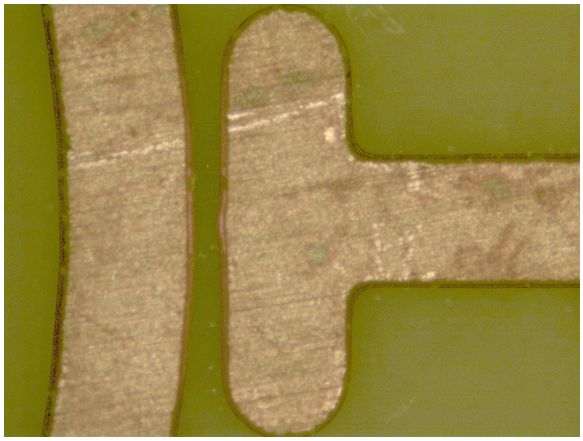

Figure 2.7: Ring resonator coupling gap.

The unloaded Q and effective permittivity of a microstrip ring resonator can be determined from the two-port response of a resonator coupled to a transmission line. [8] The effective permittivity of the structure is given in Equation 2.6 [9], and can be easily found when the ring radius of the structure and the location of each resonant peak is known. Direct measurement of the unloaded Q is generally not possible because the measurement will have some loading impact. However, as maximum transmission occurs at resonances when the impedance of the resonator is then at a minimum, it is possible to divide the resonant frequency by the 3dB bandwidth

(illustrated in Figure 2.8 and also referred to as the half-power bandwidth) of the resonant peak to find the loaded Q (Equation 2.7). The loaded Q can then be related to the unloaded Q through Equation 2.8. Lastly, the unloaded Q and guide wavelength (Equation 2.4) establish the total loss of the system (Equation 2.9). [1]

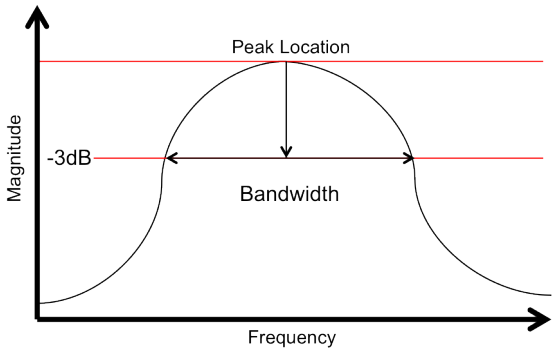

Figure 2.8: Representation of a resonant peak illustrating the 3dB bandwidth relative to center frequency.

$$\epsilon_{eff} = \frac{nc}{2\pi r f_n}^2 \tag{2.6}$$

$$Q_L = \frac{f_n}{BW_{-3dB}} \tag{2.7}$$

$$Q_0 = \frac{Q_L}{1 - 10^{L_A/20}} \tag{2.8}$$

Where L_A is the measured insertion loss at the resonance n.

$$\alpha_{tot} = \frac{\pi}{Q_0 \lambda_g} \tag{2.9}$$

$$\alpha_{tot} = \alpha_c + \alpha_d + \alpha_r \tag{2.10}$$

Radiation loss can be minimized by avoiding sharp angles or discontinuties in the microstrip transmission line, and the conductor loss (in terms of dB/m) can be approximated [2] based on the the frequency dependent conductor skin-effect resistance. Surface roughness will influence the conductor attenuation as well, but plays a negligable role and will not change as the structure is moved from air into a dielectric fluid. In this work the focus is on isolating the impact of conductor loss, substrate dielectric loss, and fluid dielectric loss.

2.5 Dielectric Material Characterization Techniques

As stated in Chapter 2, numerous techniques can be utilized to characterize dielectric fluids. When a broadband characterization is not required, the cavity perturbation technique can offer a precise single-frequency value for the complex permittivity. [4] If the deviation over frequency from a nominal value is more critical, techniques such as those used by Chretiennot et al. [13] and Errais et al. [14] may be more applicable. The technqiue used by Chretiennot et al. characterizes the response of a coplaner resonator when liquid flows through a microfluidic channel placed on top of the resonator. As the properties of the fluid deviate over time this change can be noted in the change in the response of the resonant structure. [13] The technqiue introduced by Errais et al. makes use of a differential pair, where a pristine sample is passed over one of the transmission lines of the differential pair and a contaminated sample is passed over another. Using this technique Errais et al. were able to detect small amounts of water in sulfur hexafluoride (SF6). [14]

As this work aims to achieve a precise characterization over a broad frequency range, other techniques must be explored. Open-ended coaxial probes lend themselves to the characterization of lossy fluids such as mixtures of water with methanol or ethanol [11], and as well be shown in Section 3.2, can be used to establish the complex permittivity of HFE-7100 over a broad range of frequencies. For the low-loss fluids

of interest, Novec-649 and FC-72, a combination of measurement using a high-Q microstrip ring resonator and computer-similation was used.

In the case of the microstrip ring resonator, when the fluid above and around the microstrip conductor is not air, but a lossy fluid with ϵ_r greater than one, the process of extracting ϵ_r from ϵ_{eff} is not trivial. Rather than relying on semiempirical approximations this work makes use of the finite element full-wave 3D electromagnetic solver ANSYS HFSS to fit simulation results to measurements. The use of HFSS to fit simulation results to measurements of microstrip ring resonators in air was presented by Fang et al. [9] In this process the measured value of ϵ_{eff} is matched in simulation by adjusting ϵ_r of the dielectric substrate. Similarly the Q factor can be matched by modifying the loss tangent of the substrate as well as the conductivity and surface roughness of the conductor.

Once the performance of the system in air is understood, the structure can be submerged in the fluid under test, producing a change in the value of ϵ_{eff} and the Q factor of the system. In the case of a ring resonator this is noted through shift in the resonant frequency peaks of the structure as well as their 3dB bandwidth as noted in Section 2.4. Dewdney et al. utilized this technique to characterize the polymer SU-8. [10]

A similar combination of computer aided simulation and submersion in fluid was performed by Mosalanejad et al. using an inverted patch resonator [12], a one-port structure suited to the characterization of lossy fluids. Additionally, multiple techniques can be combined, as was done by Kheir et al. through the use of a hybrid structure consisting of a ring resonator inside of a resonant cavity. This hybrid approach uses the cavitity perturbation technique to verify the results found using the ring resonator.

The technique at the center of this work makes use of a microstrip ring resonator and the finite element full-wave 3D electromagnetic solver ANSYS HFSS. The steps

comprising this technique are outlined in the flow-chart presented in Figure 2.1. An overview of the fitting process used within simulation is illustrated in Figure 3.8. Characterization of pristine fluids is covered in Section 3.3.2 and analysis of perturbed fluids can be found in Chapter 4.

Chapter 3

Dielectric Fluids Characterization

In this chapter we perform the characterization of Novec-649, FC-72, and HFE-7100. Initial DC testing below the break-down voltage of each fluid is performed followed by measurement of each fluid using an open-ended coaxial probe, establishing that HFE-7100 exhibited much greater loss than both FC-72 and Novec-649. The inability to accurately measure the loss tangent of FC-72 and Novec-649 using the coaxial probe served as the motivation for the microstrip ring resonator based characterization which is at the center of this work.

3.1 DC Characterization

When the electric field across an insulator exceeds the dielectric strength of the material, a process known as breakdown occurs, whereby the the resistance of the material is reduced and its insulating properties are compromised. [2] Using the structure presented in Section 2.1, each of the fluids of interest are placed under DC bias, producing fields approaching the values given Table 1.1.

For air the field required to produce breakdown is approximately 3 MV/m, while the dielectric strengths across a 0.1"' gap (2.54mm) are given as approximately 40kV for HFE-7100 and greater than 40kV for both FC-72 and Novec-649. Thus a field of approximately 15.75 kV/mm is required to induce breakdown. However, the tested strength was only 10kV/mm using the 0.5mm gap structure and a Keithley Model 248 High Voltage Supply with a maximum output voltage of 5kV.

Surprisingly, breakdown was observed within Novec-649 using the 0.5mm gap structure and 5kV supply after approximately ten minutes. However, it was subsequently established that the root cause for this event was excess flux that remained on the structure after lead wires were soldered to its pads. When wires were soldered onto the DC gap structures using silver solder with a flux core and subsequently cleaned using methanol no breakdown was seen in FC-72, Novec-649, and HFE-7100.

To better understand the initial breakdown event, a structure with excess flux was allowed to remain in Novec-649 for roughly five minutes. Upon removal of the structure from the fluid, a discoloration along the gap was noted (Figure 3.1). While further study is required to establish the nature of this discoloration, the assumption is that the soluble flux migrates within the fluid under the influence of the electric field, forming a conductive network over time.

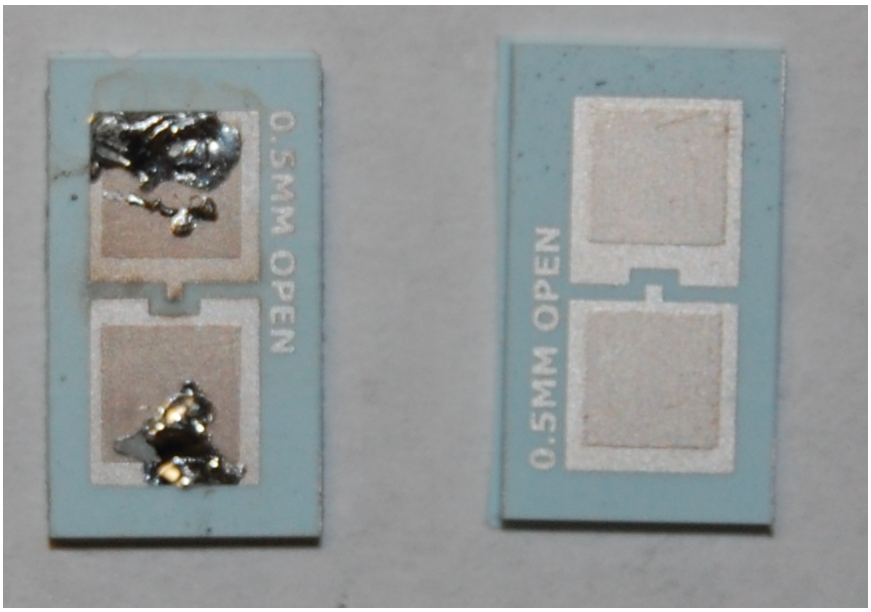

Figure 3.1: DC bias gap structures, after biasing (10kV/mm) with excess flux (left) and unused (right).

3.2 Open Coaxial Probe

The measurements in this section were made using the Agilent 85070E Performance Probe with an Agilent N4693A electronic calibration unit connected to the Agilent N5227A PNA Network Analyzer using a 2.4mm cable. While the basis of the one-port measurement made by the performance probe was outlined in Section 2.2, additional considerations must be made in terms of calibration and measurement setup. The calculation of the complex relative permittivity done in software carries the assumption that the sample has effectively infinite thickness, is non-magnetic, isotropic, homogeneous, and that no air gaps or bubbles are present. [16] For the measurements performed in this work, satisfying these assumptions requires that the volume of fluid under test and container size are large enough to avoid electromagnetic reflections from the edge of the sample or the sample holder. This was accomplished by using a 20mL beaker with the probe tip inserted at the center of the opening and at least three centimeters below the surface of the fluid. Calibration (See Appendix A) of the performance probe consisted of a measurement of air followed by a measurement made while the probe is shorted against a metalic block provided by Agilent Technologies. Lastly a measurement of de-ionized water at a known temperature is performed. Using these three measurements, the software provided by Agilent Technologies produces error terms that extend the calibration plane from the network analyzer to the probe tip itself. By storing these error terms, the electronic calibration unit is able to correct for calibration drift over time as measurements are made.

The permittivities of de-ionized (DI) water, air, and methanol are well documented over a broad frequency range and provided as reference values by Agilent Technologies. By measuring these fluids (Figure 3.2) and comparing them to their known values the validity of the calibration can be determined. While all measurements were performed up to 50GHz (indicated by the date 6-19-13), an earlier set of

measurements (performed on 6-5-13) was produced for water, methanol, and HFE-7100 using a calibration up to 20GHz. The similarity between both sets of measurements establishes a confidence in the calibration process and the measurement setup.

Measurements of FC-72 and Novec-649 (Figure 3.4) confirm a relative permittivity similar to the dielectric constant provided by the manufacter through datasheets, but report a negative loss tangent. Rather than assuming that the fluid exhibits gain, the possibility of calibration or instrumental error was discussed with Agilent [17]. A sample was provided to Agilent, allowing an experienced applications engineer to reproduce the measurement. The results produced by Agilent exhibited the same negative gain, indicating a limited instrumental resolution rather than a calibration error.

The values of ϵ_r and $\tan\delta$ obtained for HFE-7100 using the probe (Figure 3.3) were used as the initial fluid material properties in simulations of transmission line structures submerged within HFE-7100.

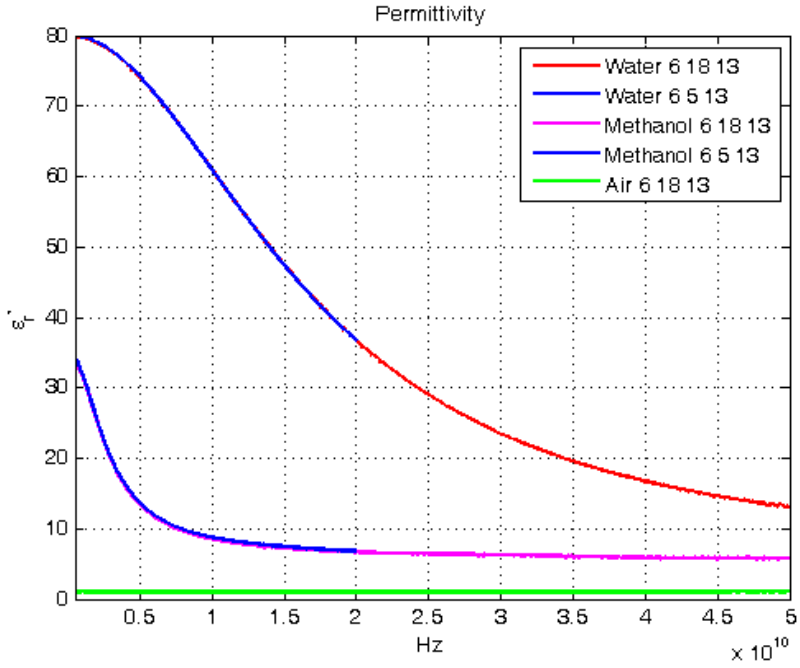

(a) Relative permittivities of measurement standards.

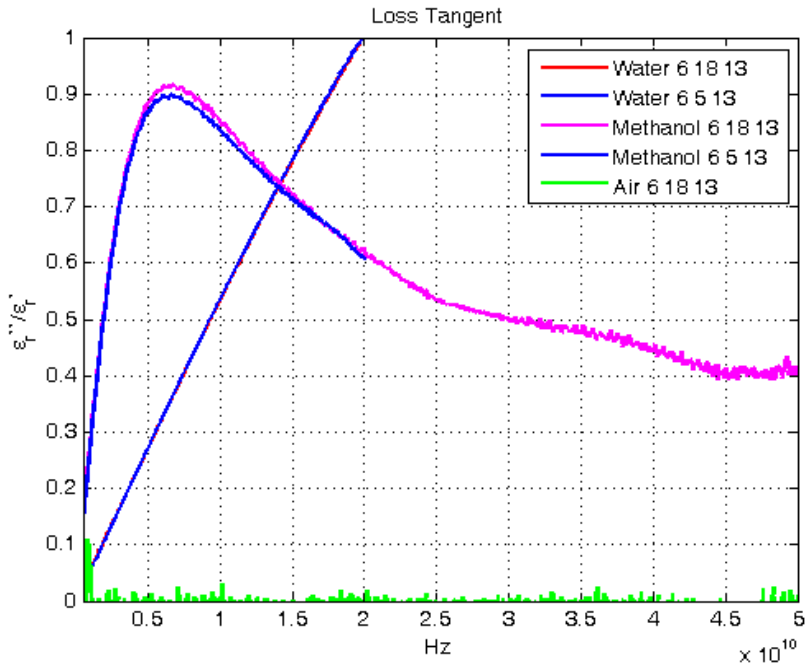

(b) Loss tangents of measurement standards.

Figure 3.2: De-Ionized water, methanol, and air as measured using the Agilent 85070E Performance Probe.

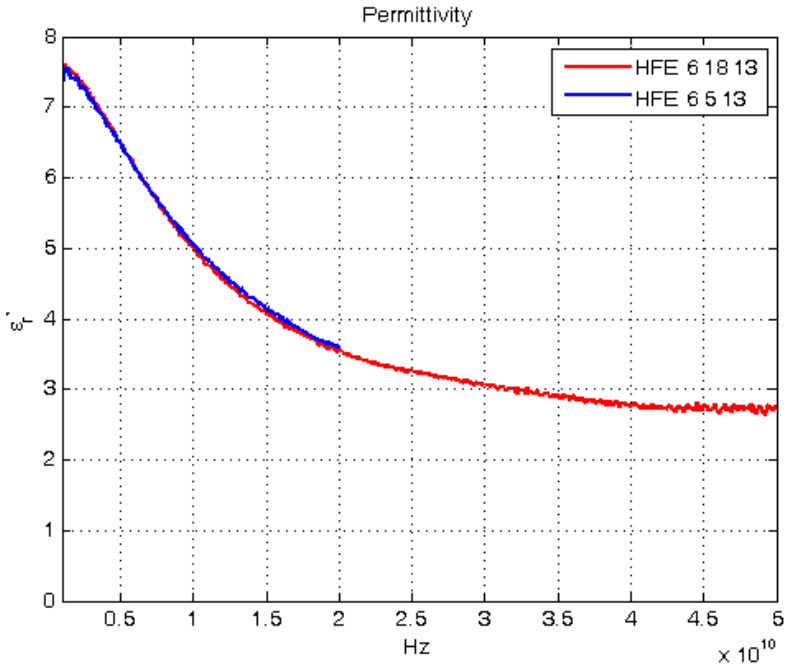

(a) Relative permittivity of HFE-7100.

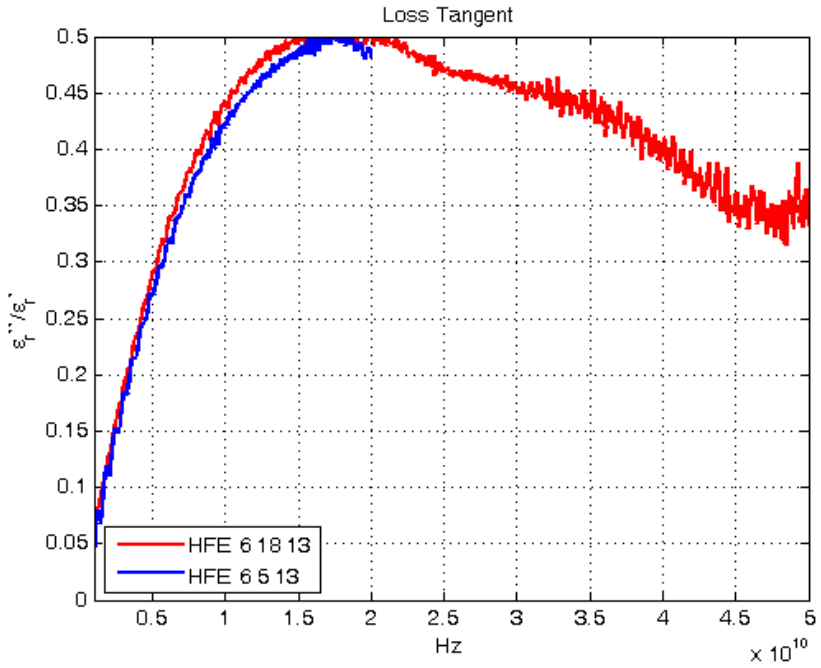

(b) Loss tangent of HFE-7100.

Figure 3.3: Measurement of HFE-7100 using the Agilent 85070E Performance Probe.

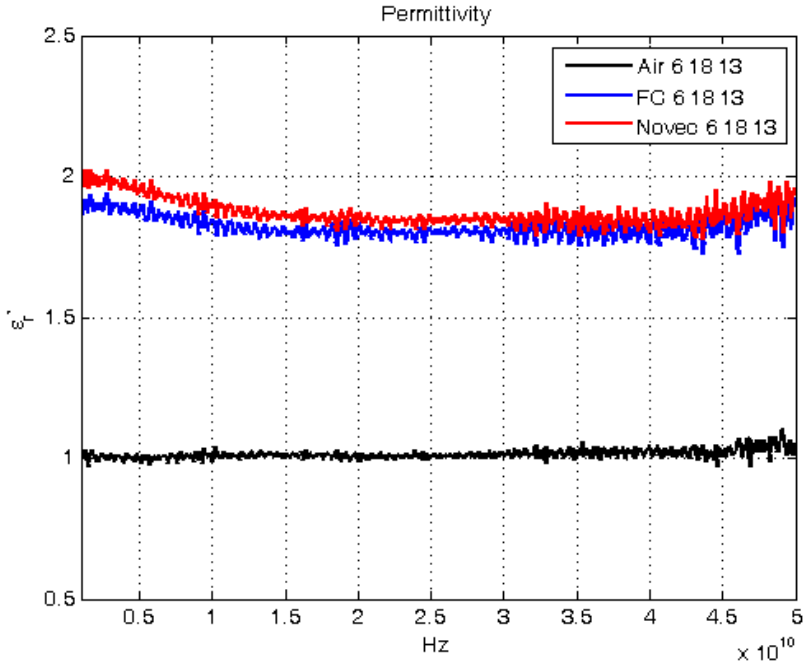

(a) Relative permittivities of low-loss fluids.

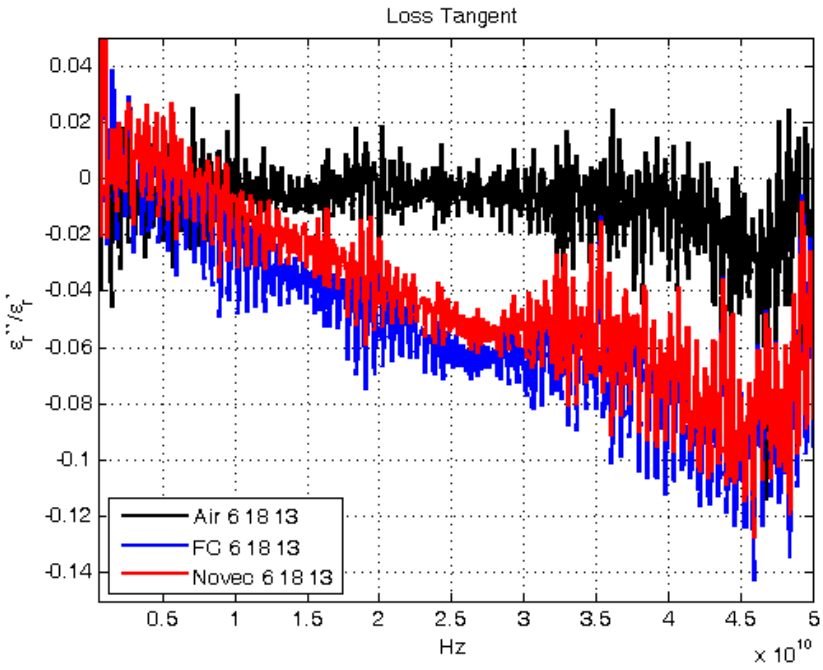

(b) Loss tangents of low-loss fluids.

Figure 3.4: Measurement of FC-72, Novec-649, and air using the Agilent 85070E Performance Probe.

3.3 Microstrip

The inability to accurately measure the loss tangent of FC-72 and Novec-649 using the Agilent 85070E Performance Probe served as the motivation for the microstrip based characterization detailed further in this section. Subsection 3.3.1 makes use of microstrip transmission line structures, which can be used to establish an approximate loss tangent for each fluid of interest relative to air. However, to precisely and accurately characterize both Novec-649 and FC-72 a microstrip ring resonator approach is presented in Subsection 3.3.2.

Both microstrip transmission line and microstrip ring resonator structures are fabricated using copper metalization on a Megtron6 (M6) dielectric substrate and measured using an Agilent N5227A PNA Network Analyzer. A thru-reflect-line (TRL) calibration kit (See Appendix B) was fabricated onto the same substrate, and the 0.433" ($\sim$11mm) line used in Subsection 3.3.1 is one of the lines comprising the TRL calibration kit.

Substrate Height (d or h)	9.54 mil	242.32μm
Conductor Thickness (t)	2.68 mil	68.10μm
Line Width (W)	21.4 mil	543.56μm

Table 3.1: Microstrip dimensions

The depth to which each of the structures were submerged is shown in Figure 3.5, where a red line is used to indicate the fluid surface. It should be noted that the connectors used (Molex 73387-0020) feature gaskets that do not allow the fluid to enter the connector.

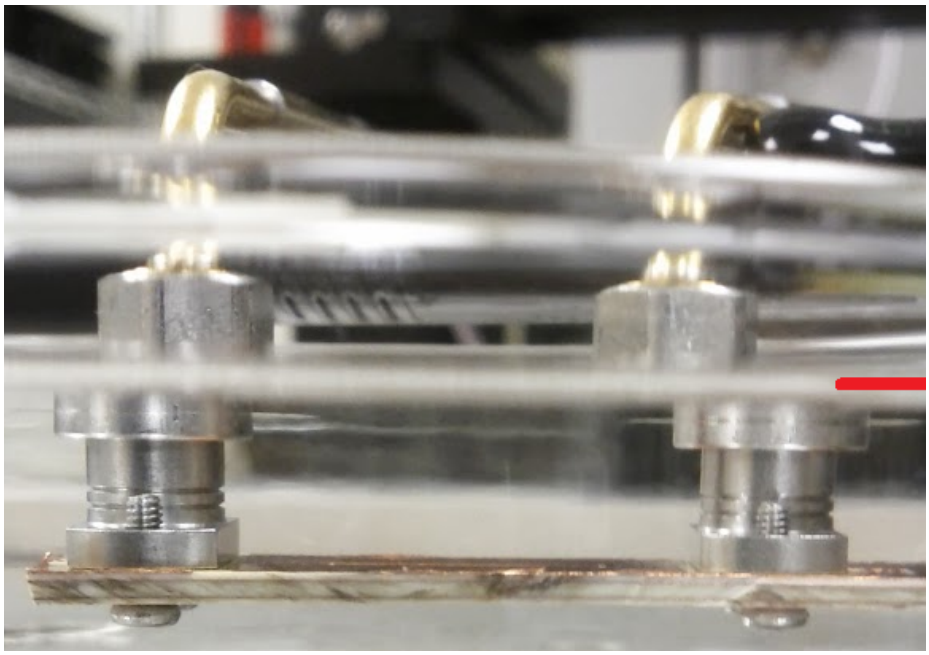

Figure 3.5: Microstrip transmission line submerged in fluid. The fluid level is indicated with the red line on the right side of the photograph.

3.3.1 Microstrip Transmission Lines

The values provided in Table 1.1 show that Novec-649 and FC-72 have very similar dielectric constants, however the loss tangents of both Novec-649 and FC-72 are unknown. It is assumed that the unknown loss tagents are greater than the loss tangent of air and less than the loss tangent of HFE-7100 found using the open-ended coaxial probe. The physical dimensions of the microstrip are known, and the dielectric constant of the M6 substrate is known to be approximately 3.6. A calibrated measurement of the transmission line (with length 0.433" or ∼11mm) in air is matched using simulation, establishing the frequency dependent complex permittivity of the M6 substrate. With this basis it possible to establish an approximate dielectric loss tangent for FC-72 and Novec-649 within simulation by matching measurements taken when the transmission line is submerged in fluid.

Figure 3.6 illustrates that when the calibration was performed with the substrate in air (shown in black) prior to the measurement of lines submerged in fluid, a distinct high-loss region was present from 45-50GHz. By using the same calibration kit but performing the calibration with the TRL structures submerged in the fluid of interest less attenuation was observed. The latter measurements are illustrated in Figure 3.6 in color. It should be noted that as the calibration kit was designed for use in air there are portions of the return loss that exhibit gain. In this work we extrapolate through this trend.

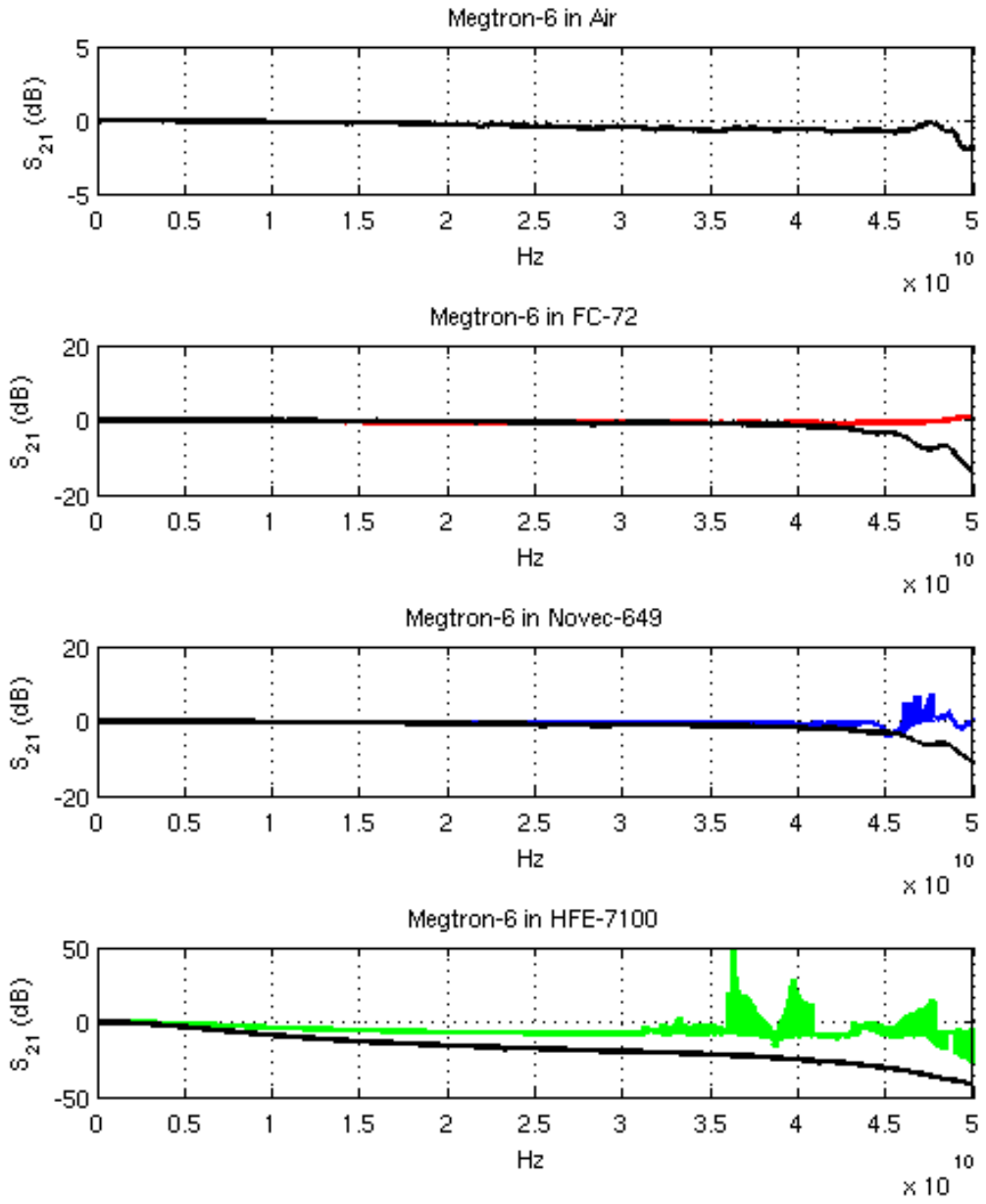

Figure 3.6: Measured microstrip transmission line insertion loss. Measurements made after an air based TRL calibration are shown in black while measurements made using a calibration in which the same TRL structures were submerged in the fluid of interest are shown in color.

3.3.2 Microstrip Ring Resonator

The microstrip ring resonator structure introduced in this section is based on the theory introduced in Section 2.4 and implemented using the same microstrip dimensions (Table 3.1) and TRL calibration introduced in Subsection 3.3.1. Additionally, the radius of the ring is 342.64mil (∼8703.06μm), and the coupling gap 2.7 was optically measured at 3.75 mil (95.25μm), althought it was designed to be 5 mil (127μm). A parametric sweep of the gap size was performed, establishing that the first and most prominent peak (Figure 3.9) could be matched in simulation only when using the more narrow gap size.

While calibration in air was performed when measuring the structure in air for the purpose of dielectric substrate characterization, all measurements used to characterize the fluid of interest were performed after a calibration within the specific fluid of interest.

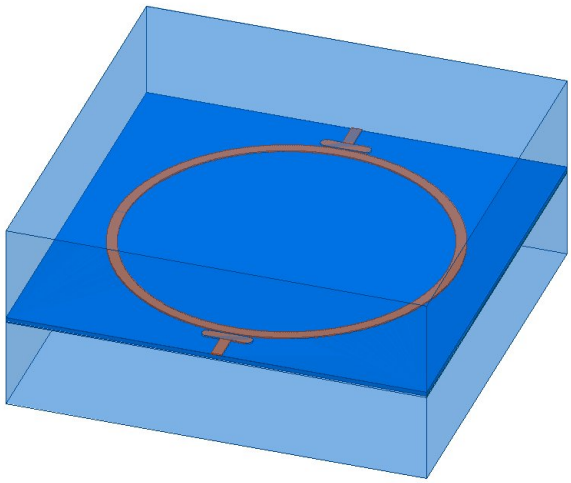

Figure 3.7: A 3D view o the model of the microstrip ring resonator surrounded by air or a dielectric fluid was used in HFSS simulations.

In this work an empirical process was used to fit the insertion loss (S_{21}) of the simulated ring resonator to the insertion loss found through calibrated measurements of the ring resonator structure in air and fluid.

The fitting process was aided by a heuristic; if the permittivity at a specific frequency was too high, the peaks were observed to move down in frequency. Conversely, if the permittivity of the material used in simulation was lower than expected the peaks were found to move up towards a higher frequency.

The finding the loss tangent of the material of interest involved increasing or decreasing the loss tangent of the material until the attenuation of the peaks in simulation matched the results in measurement. The conductivity of the copper metalization was fixed at 5×10^7 S/m with no surface roughness.

An overlay of the simulated and measured insertion loss is shown in Figure 3.9, where measured data are shown in color while the simulated insertion loss is indicated using a thin black line. The extracted relative permittivities and loss tangents are shown in 3.10 and 3.11 and in the case of Novec-649, FC-72, and HFE-7100 compared to results found using the open coaxial probe. Reduced resolution datafiles of the relative permittivies and loss tangents shown in Figures 3.10 and 3.11 are provided in Appendix E.

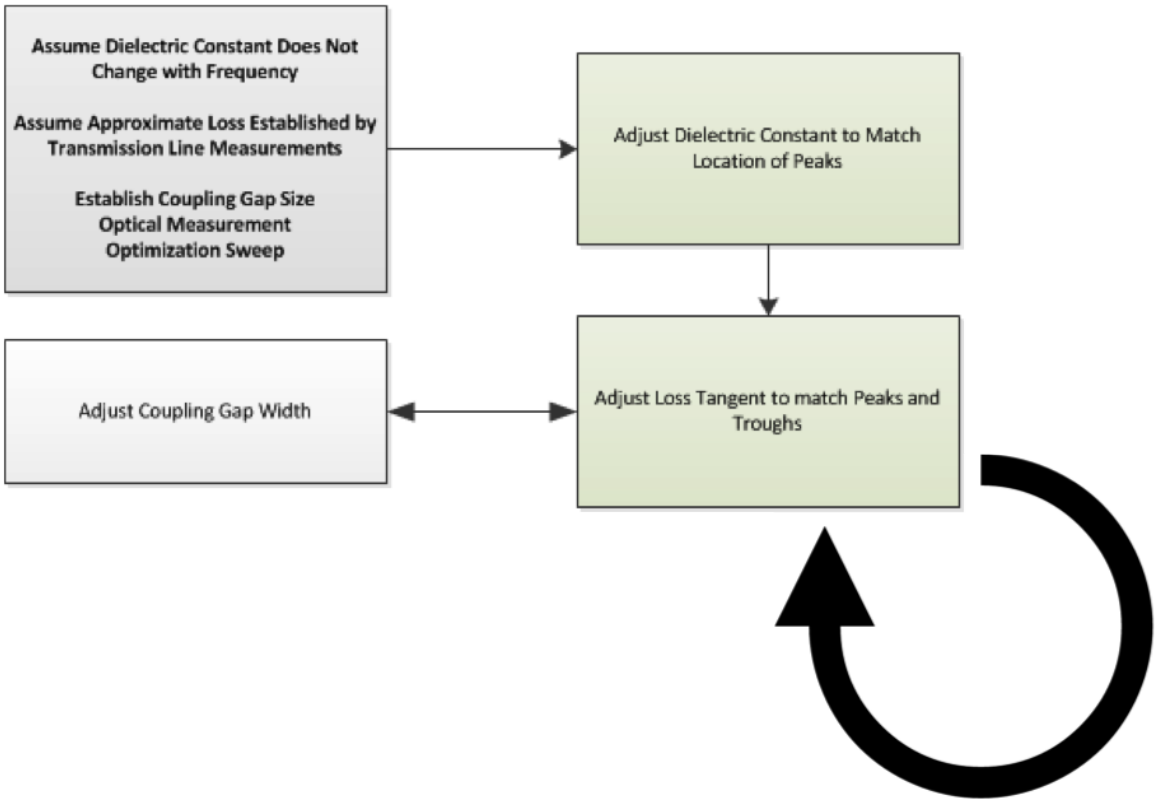

Figure 3.8: A flow chart of the empirical technique used to fit simulation results to measurement results.

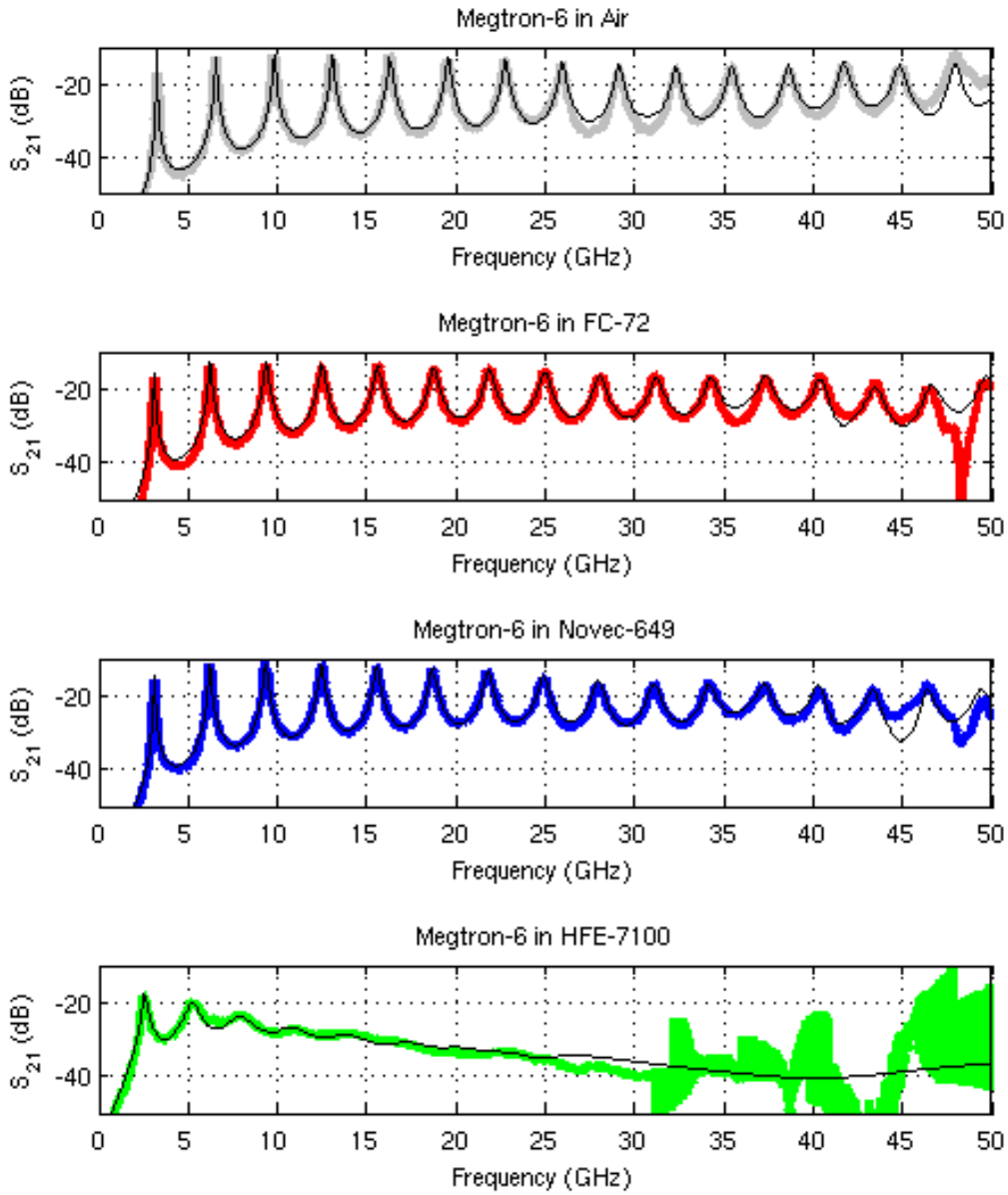

Figure 3.9: Measurement and simulation comparison of ring resonator in all fluids.

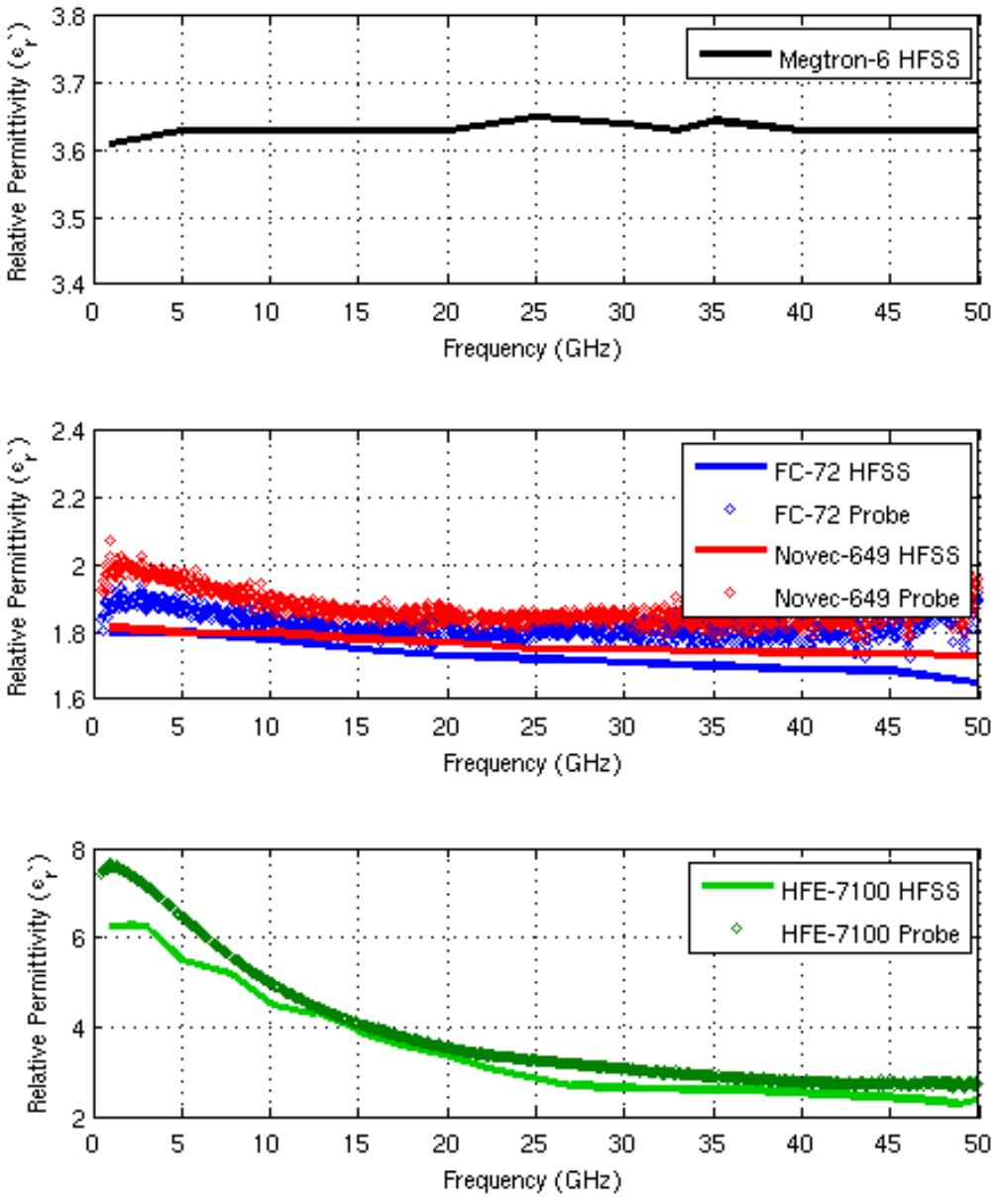

Figure 3.10: Substrate and dielectric fluid permittivity.

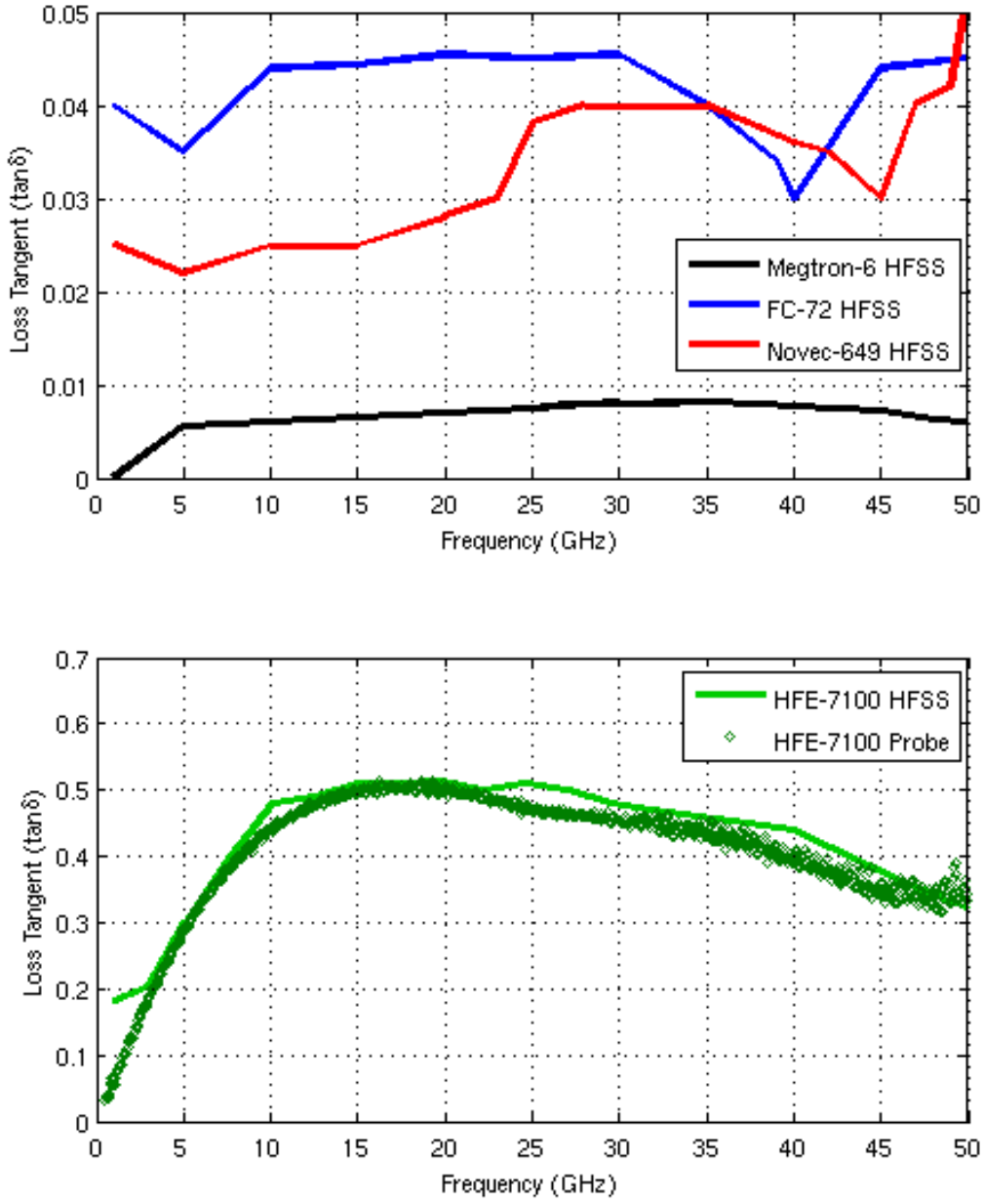

Figure 3.11: Substrate and dielectric fluid loss tangent

Chapter 4

Contamination Study

In this chapter the open-ended coaxial probe and microstrip ring resonator used to characterize pristine dielectric fluids are used to analyze fluids that has been purposely perturbed by means of contamination. In applications where commodity electronic systems have been submerged in a dielectric fluid it is possible that certain materials will begin leaching chemicals (i.e. plasticizers, colorants, antistatic additives) into the cooling fluid. These and other contaminents can impact both the thermal and dielectric properties of the cooling fluid. Ideally, these contaminants can be detected and characterized in low concentrations, allowing a similar in-situ measurement to indicate contamination events before they negatively impact the electronic system.

Compounds of with a low solubility in the dielectric fluids can be extracted from a solid using a Soxhlet extraction. This extraction process makes use of a refluxing solvent which repeatedly washes the solid, extracting the contaminant compound into the flask [18]. Typically, a Soxhlet extraction is only required where the desired compound has a limited solubility in a solvent, and the impurity is not readily miscible in that solvent. Using the soxhlet method, numerous contaminants were analyzed.

While there is little confidence in the absolute measurement reported by the coaxial probe, it should be noted that Natural Rubber (Sample #25) is outside of the range of error in 4.2. Indicating that this contaminent has a greater impact on the dielectric cooling liquid than other contaminents.

Measurement of the same set of fluids using the microstrip ring resonator showed that Novec-649 used in soxlet extraction with Natural Rubber (Sample #25) resulted

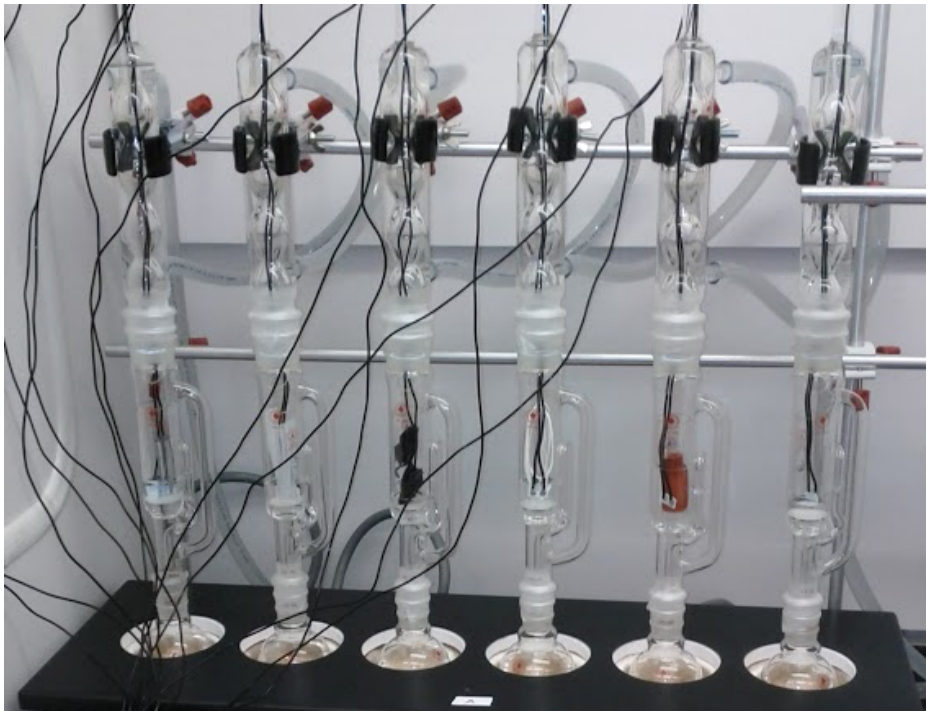

Figure 4.1: Soxhlet Extraction Tubes

in a measured value outside of the range of error of the measurement. When simulation of the contaminated fluid was matched to measurement (over the limited range of 10-20GHz) and compared to pristine Novec-649, an increase in the loss tangent by 0.035 (from 0.025 to 0.06) was noted. Additionally an increase of 0.1 in the relative permittivity (from 1.8 to 1.9) was observed over this limited range.

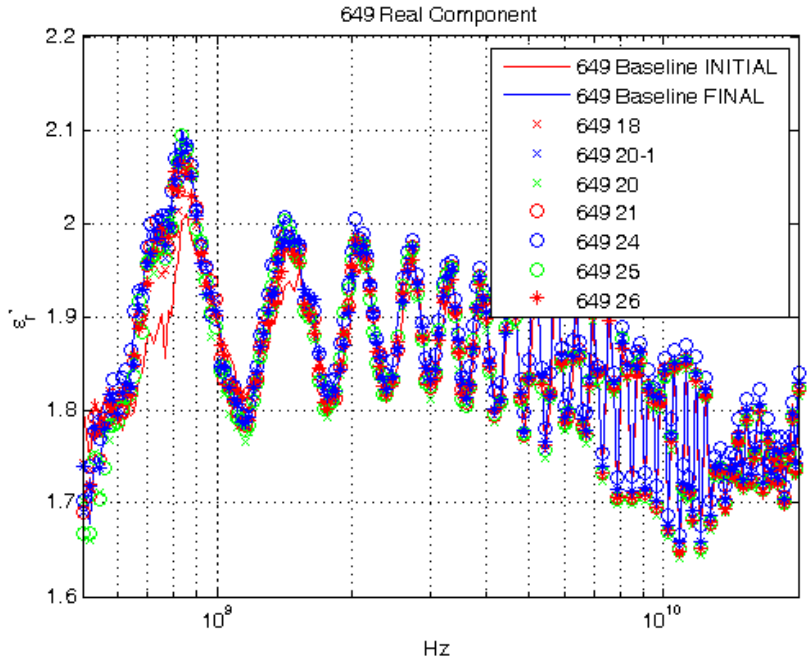

(a) Relative Permittivities of Measurement Standards

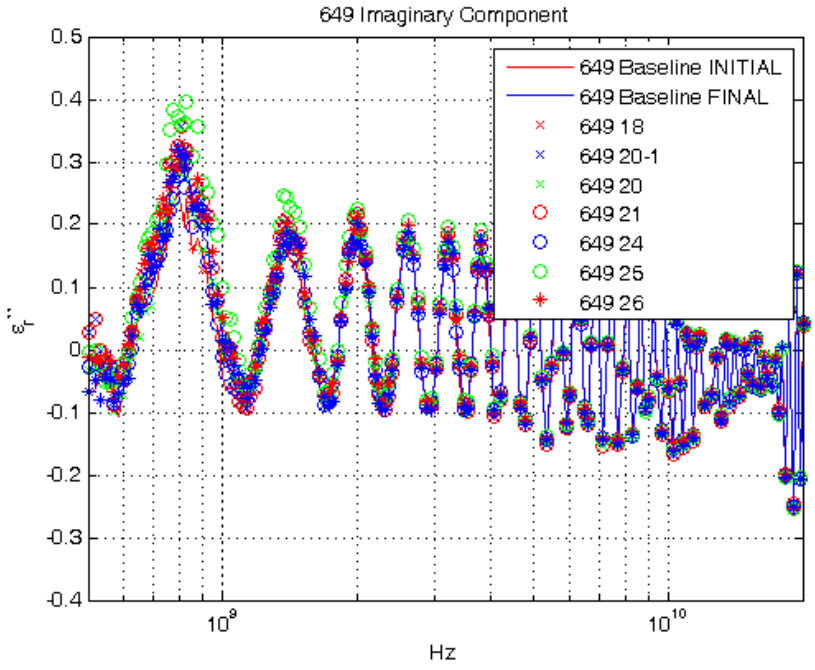

(b) Loss Tangents of Measurement Standards

Figure 4.2: Real and imaginary component of probe measurement of perturbed fluids. Note that the imaginary component of Natural Rubber (Sample #25) falls outside of the what could be considered the range of error.

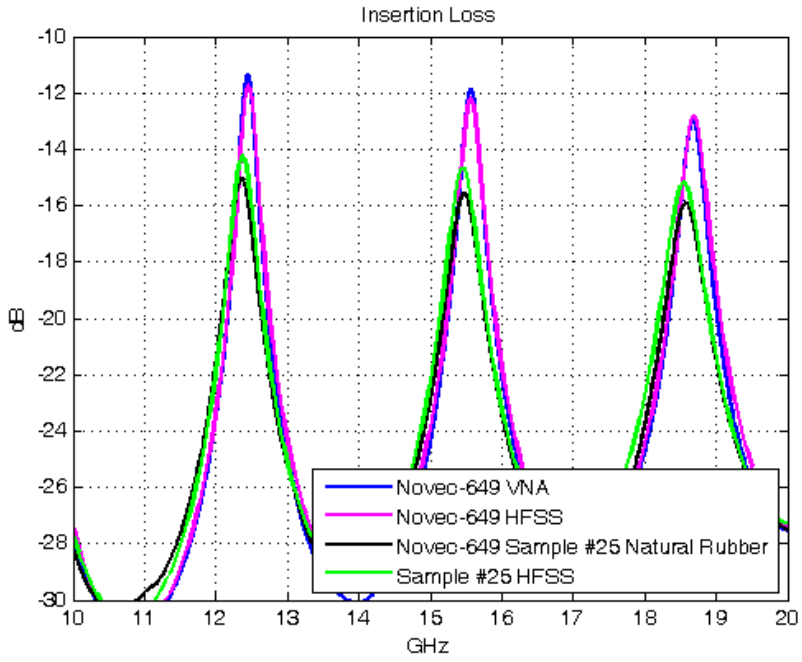

Figure 4.3: Impact of natural rubber contaminent.

Chapter 5

Conclusions and Future Work

Characterization of Novec-649, FC-72, and HFE-7100 using a ring resonator structure yielded a broadband complex permittivity that, in the case of Novec-649 and FC-72, the open coaxial probe was unable to do. Additionally, while the contaminant Natural Rubber in Novec-649 did appear outside of the range of measurement error when perturbed samples were measured with the open coaxial probe, the ring resonator based technique outlined in this work allowed for the extraction of the complex permittivity of a contaminated fluid. It should be noted that as only one ring resonator structure was used, it is possible that the relative permittivity and loss tangents are actually an over-fit to the structure.

It should be noted that when the fluid permittivity is considerably different from air in terms of relative permittivity or loss, a second iteration for characterization may be required, as illustrated in Figure 5.1. This second iteration should consider the extracted complex permittivity of the dielectric fluid of interest when designing the calibration kit, yielding lines with a better match to 50Ω. A second iteration of structures should also include consideration for the width of the coupling gap of the ring resonator.

In order to carefully study the transition from cable to microstrip transmission line a measurement using time domain reflectometry (TDR) may provide insight into creating better matched lines. However, such a TDR measurement could only be executed with transmission line structures, as measurements of the ring resonator structure requires the broad frequency sweep generated by a VNA.

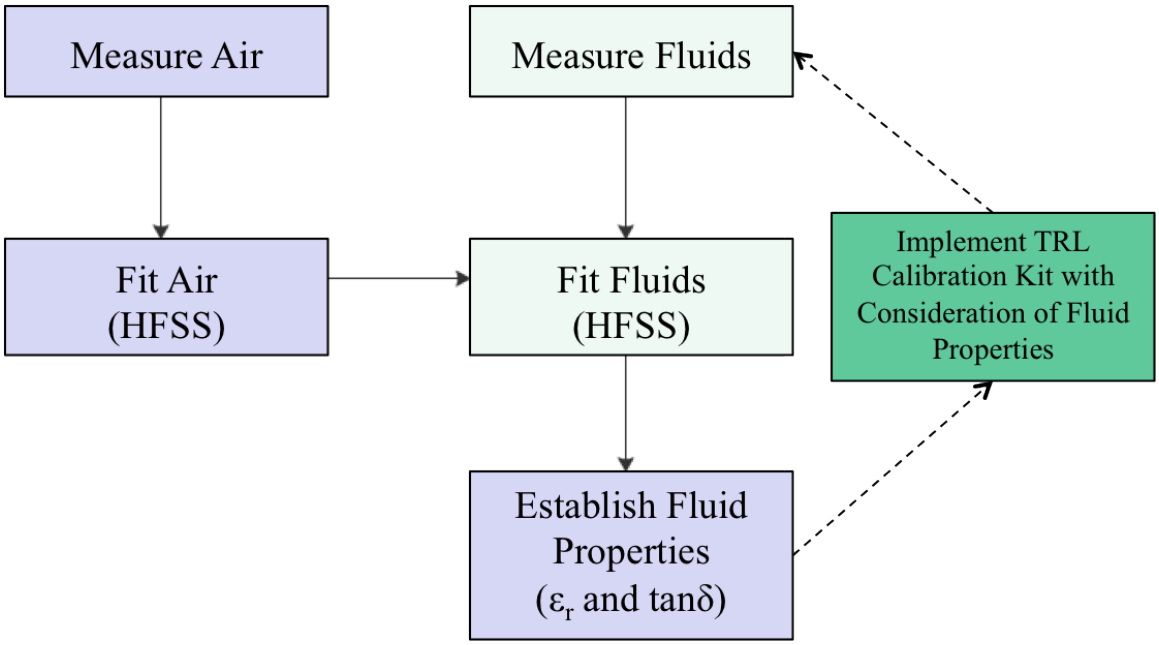

Figure 5.1: Improvement to the complex permittivty extraction technique using measurement and simulation.

Additionally, measurement confidence could be increased by complementing ring resonator measurements with cavity perturbation measurements at one or more frequencies, as was done by Kheir et al. [15]

5.1 Numerical Optimization

The empirical fitting of simulated insertion loss to measured insertion loss could be improved using a numerical technique in which the Q factor and effective permittivity are directly calulated and resulting error is used to automatically adjust the material properties used in simulation.

Relative Permittivity	If the simulated peak is at a lower frequency than the measured peak then ϵ_r is too high. If the simulated peak is at a higher frequency than the measured peak then ϵ_r is too low.
Loss Tangent	Increasing the loss tangent will result in a broadening of the peaks and will lower the insertion loss seen at the troughs.
Coupling Gap	The structure should be loosely coupled. As the gap is adjusted within simulation the first resonant peak may disappear or become more tightly coupled. For this reason it is crucial to use optical techniques as well as a profilometer to ensure that the modeled gap is an accurate representation of the measured gap.

Table 5.1: Heuristics applied within the empirical fitting process.

While the fit of the simulated return loss (Figure 3.9) does appear to be a good match, when the two are compared numerically (Figure 5.2 and Figure 5.3) it becomes clear that a better match can be made. The source code used to extract these values provided in Appendix D and is based on the equations introduced in Section 2.4. The numerical fitting of the values shown in Figures 5.2 and 5.3 should result in a more precise extraction of the complex permittiy than was provided by fitting he simulated return loss shown in Figure 3.9.

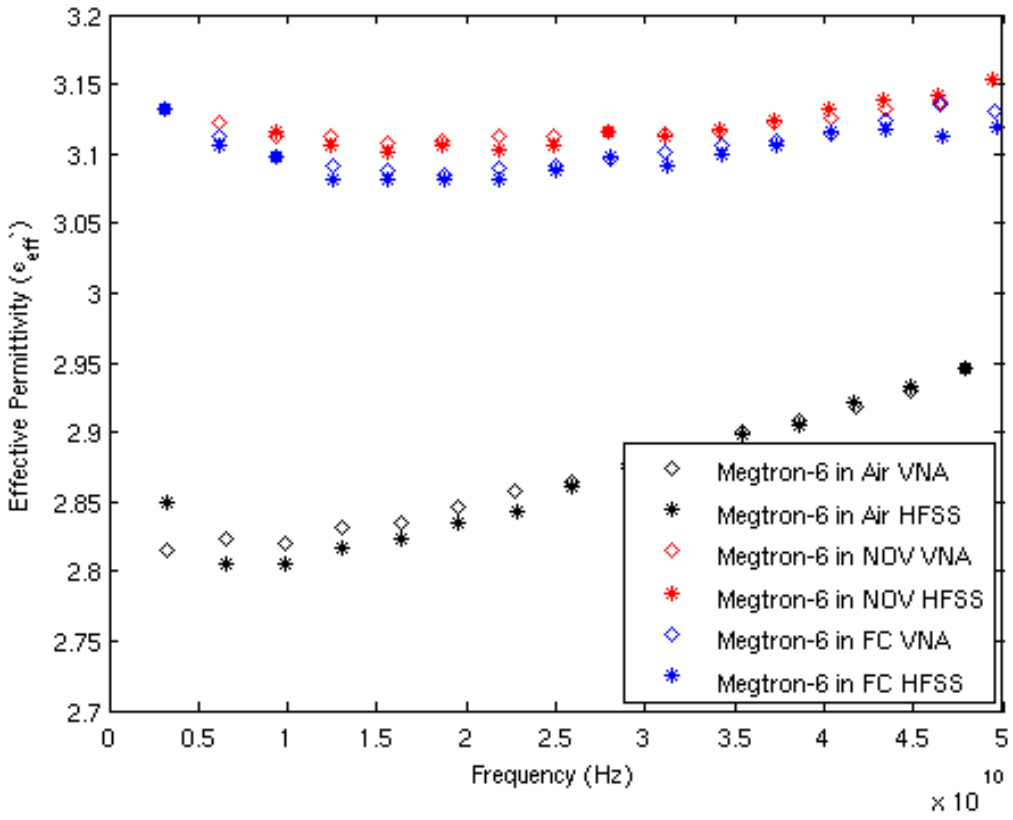

Figure 5.2: Comparison of the effective permittivity between measurement and simulation.

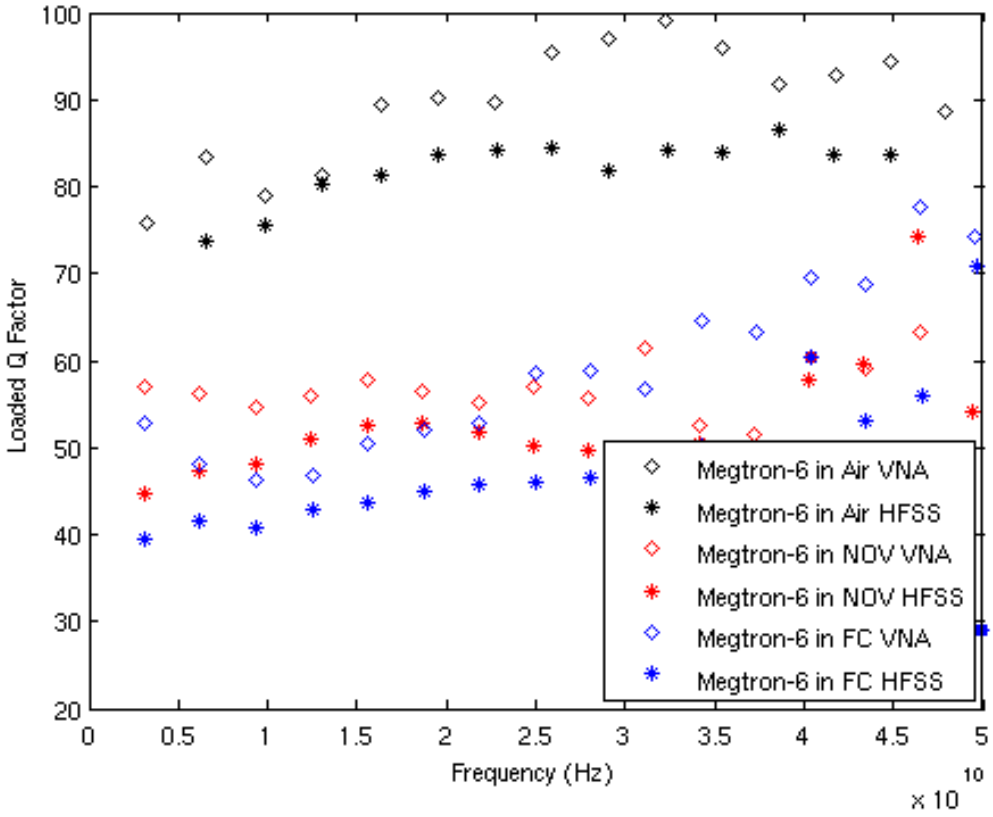

Figure 5.3: Comparison of the loaded Q Factor between measurement and simulation.

5.2 Characterization of Dielectric Fluids at Elevated Temperatures

All measurements presented within this work were peformed at room temperature. However, a more thorough characterization technique would take into consideration the impact of both low- and high-temperatue fluids – with a particular focus on elavated temperatues.

At a temperaure approaching 50° FC-72, Novec-649, and HFE-7100 will begin to boil. [5] [7] [6] The characterization of boiling fluids would require an enclosure that can allow boiling fluid to condense so as to minimize fluid losses while mainining an ambient pressure. Additionally the inverted microstrip ring resonator characterization structure should be directly exposed to bubbles that form while the fluid is boiling. Such a characterization would most closely model the target application of each dielectric fluid as it was stated in the introduction.

References

[1] G. Zou, H. Gronqvist, J. Starski, and J. Liu, "Characterization of liquid crystal polymer for high frequency system-in-a-package applications," *Advanced Packaging, IEEE Transactions on*, vol. 25, no. 4, pp. 503–508, 2002.

[2] S. Wentworth, *Applied Electromagnetics: Early Transmission Lines Approach*, ser. Wiley series in electrical and computer engineering. Wiley, 2007. [Online]. Available: http://books.google.com/books?id=kP9_QgAACAAJ

[3] A. Technologies, "Microwave dielectric spectroscopy workshop." Agilent Technologies, 2004.

[4] S. Begley, "Electromagnetic properties of materials: Characterization at microwave frequencies and beyond." Agilent Technologies.

[5] 3M, *Fluorinert Electronic Liquid FC-72*, 98th ed., May 2000.

[6] ——, *Novec Engineered Fluid HFE-7100 for Heat Transfer*, 98th ed., January 2002.

[7] ——, *Novec 649 Engineered Fluid*, 60th ed., September 2009.

[8] D. Pozar, *Microwave Engineering*. Wiley, 2011. [Online]. Available: http://books.google.com/books?id=Zys5YgEACAAJ

[9] X. Fang, D. Linton, C. Walker, and B. Collins, "Dielectric constant characterization using a numerical method for the microstrip ring resonator," *Microwave and Optical Technology Letters*, vol. 41, no. 1, pp. 14–17, 2004. [Online]. Available: http://dx.doi.org/10.1002/mop.20031

[10] J. Dewdney and J. Wang, "Characterization the microwave properties of su-8 based on microstrip ring resonator," in *Wireless and Microwave Technology Conference, 2009. WAMICON '09. IEEE 10th Annual*, 2009, pp. 1–5.

[11] J.-Z. Bao, M. L. Swicord, and C. C. Davis, "Microwave dielectric characterization of binary mixtures of water, methanol, and ethanol," *The Journal of Chemical Physics*, vol. 104, no. 12, pp. 4441–4450, 1996. [Online]. Available: http://link.aip.org/link/?JCP/104/4441/1

[12] M. Mosalanejad, G. Moradi, and A. Abdipour, "An inverted microstrip resonator for complex permittivity measurement of medium loss liquids using 3d-fdtd simulation," in *Microwave Symposium (MMS), 2010 Mediterranean*, 2010, pp. 407–410.

[13] T. Chretiennot, D. Dubuc, and K. Grenier, "A microwave and microfluidic planar resonator for efficient and accurate complex permittivity characterization of aqueous solutions," *Microwave Theory and Techniques, IEEE Transactions on*, vol. 61, no. 2, pp. 972–978, 2013.

[14] A. Errais, M. Frechette, T. Sakakibara, and J. Goyette, "Development of a differential microwave system to measure traces of water in sf6," in *Transmission Distribution Conference and Exposition: Latin America, 2006. TDC '06. IEEE/PES*, 2006, pp. 1–4.

[15] M. S. Kheir, H. Hammad, and A. Omar, "Measurement of the dielectric constant of liquids using a hybrid cavity-ring resonator," in *PIERS Proceedings*, 2008.

[16] A. Technologies, *Agilent 85070E Dielectric Probe Kit 200MHz to 50GHz*, jan 2012.

[17] A. Westwood, Personal Communication", November 2012.

[18] R. S. of Chemistry, "Soxhlet extraction," *The Interactive Lab Primer*. [Online]. Available: http://www.chem-ilp.net/labTechniques/SoxhletExtraction.htm

Appendix A

Coaxial Probe Calibration

Agilent's software requires a three part calibration. An e-cal unit (Agilent N4693A) was used during calibration and measurement, allowing the VNA to re-calibrate the system before each measurement, nearly eliminating cable instability and calibration drift.

1. Measure Air
2. Measure shorting block
3. Measure DI water at given temperature 20.5 °C

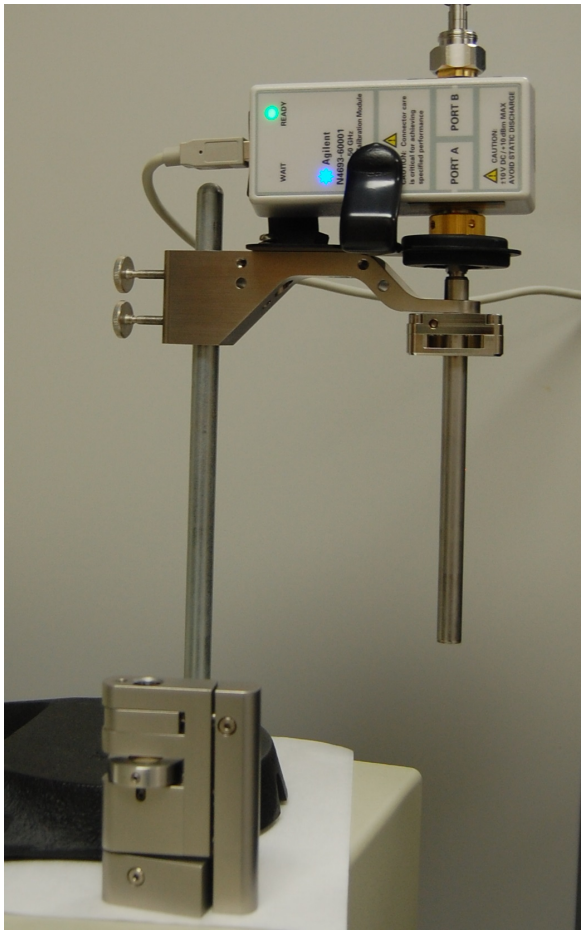

Figure A.1: Agilent probe and calibration short.

Appendix B

Microstrip Calibration and Fluid Immersion Considerations

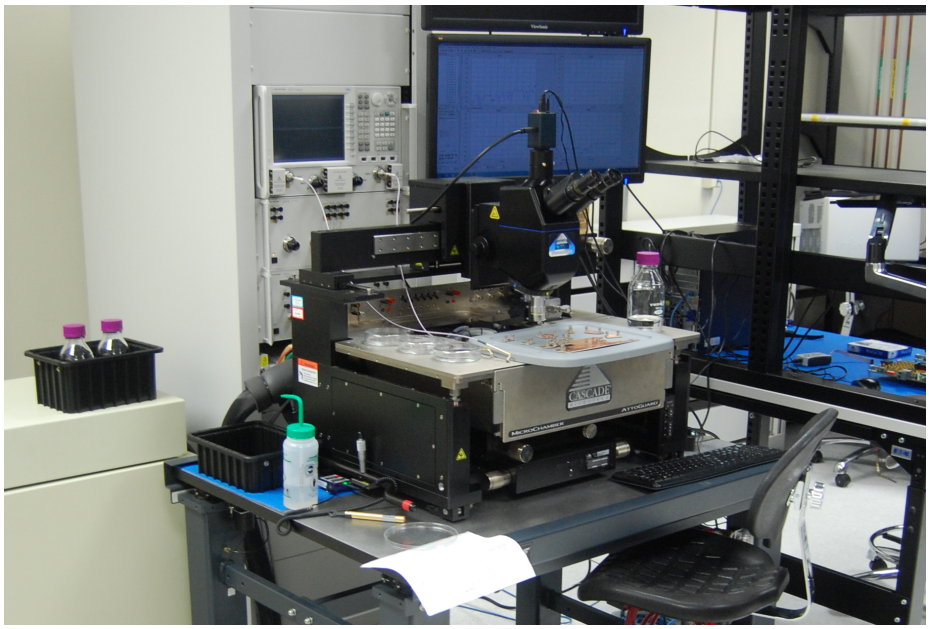

Figure B.1: Photograph of probe station and network analyzer.

The frequency range and dynamic range of the vector network analyzer (VNA) make it attractive for measuring broadband structures like the ring resonator used in this work. A thru-reflect-line (TRL) calibration kit for M6 technology was used to eliminate unwanted effects of cables, connectors, and feedlines, effectively moving the calibration plane onto the edges of the microstrip; past the 2.4mm Molex 73387-0020 connectors and previously designed and verified signal launch structures. Measurement and calibration was done from 10MHz to 50GHz (5000 samples) with intermediate frequency (IF) bandwidth 500Hz and no averaging. It should be noted that in addition to the THRU and Line structures, reflection OPEN and matched LOAD structures were present on the calibration kit and used in calibration. When

performing the initial air calibration, or creating a modified calibration kit (for use while submerged in fluids) a forward and reverse measurement of each line is required – these steps as well as the creation of a new calibration kit are managed by the Agilent Physical Layer Test System (PLTS).

1. Port 1 OPEN, Port 2 OPEN
2. Port 1 LOAD, Port 2 LOAD
3. THRU (0.5 in)
4. Line 1 (2.167 in)
5. Line 2 (0.433 in)
6. Line 3 (0.087 in)
7. Line 4 (0.017 in)

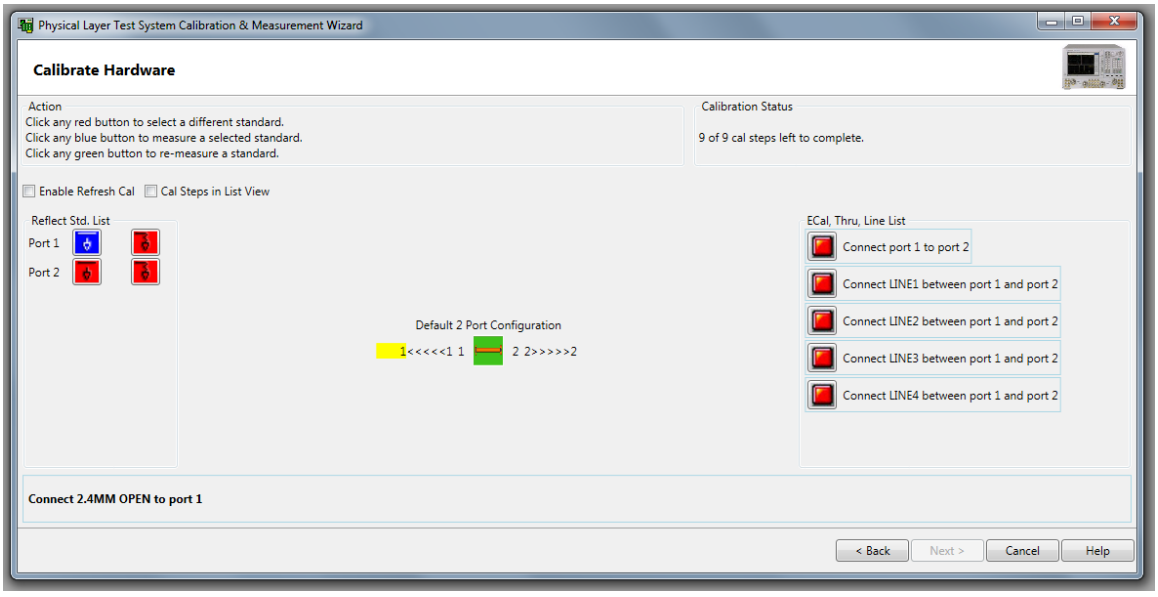

Figure B.2: Agilent PLTS calibration steps.

A comparison of the scattering parameters measured for the ring resonator in air with and without calibration is shown in B.3(a), indicating that calibration introduced

gain in the 45-50GHz range. Gain was not seen when the structure was measured in Novec-649 using an air-based calibration. However, a small amount of gain can again be seen in the return loss of the resonator when calibration was done within Novec-649. As was the case with the microstrip transmission line measurements in 3.6, we ignore and extrapolate through this trend.

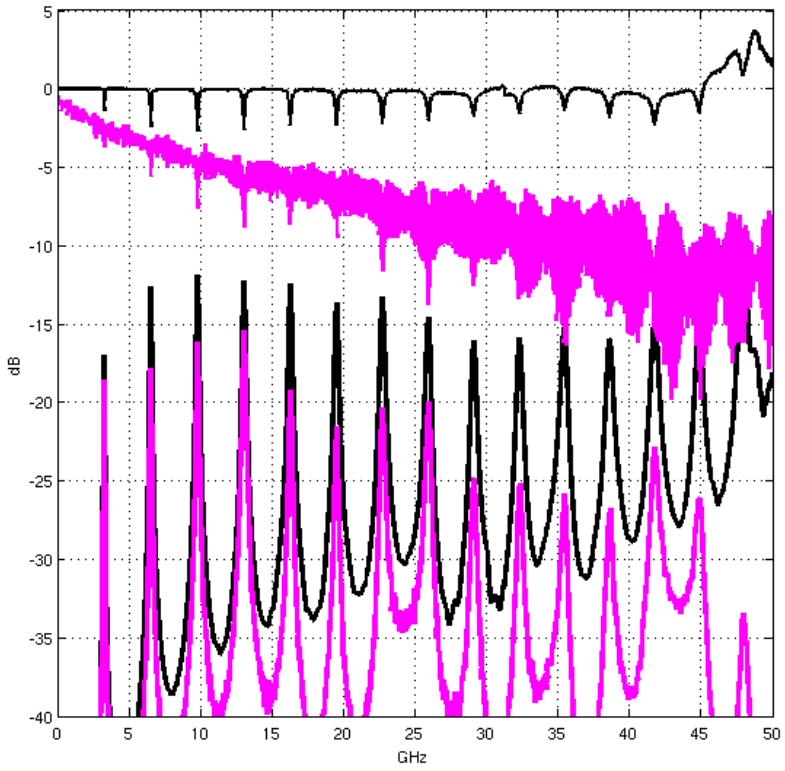

(a) Measurement of R5 in air up to 50GHz, with TRL calibration (black) and without (magenta) calibration.

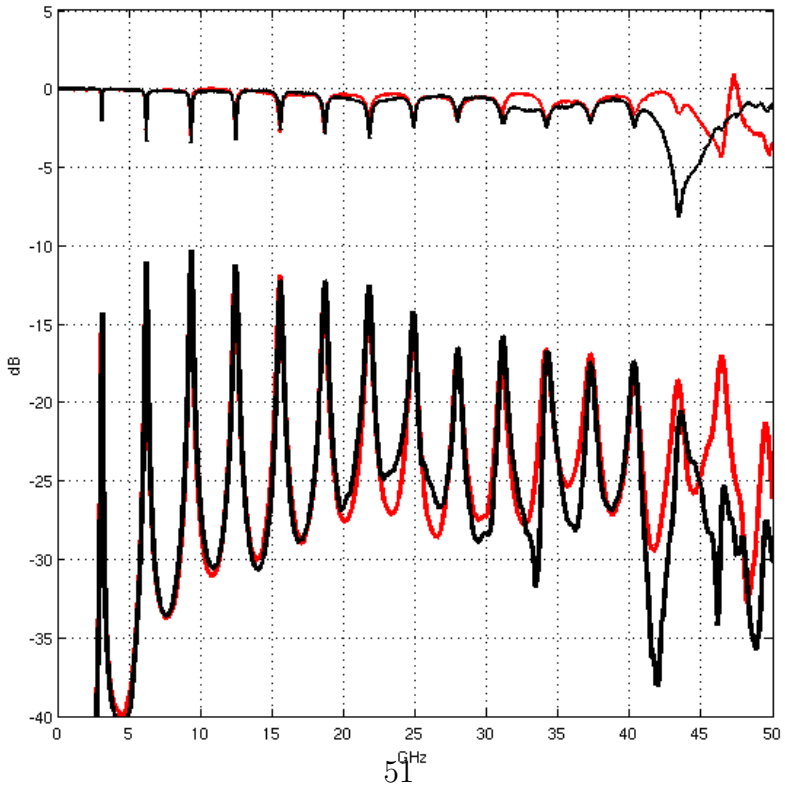

(b) Measurement of R5 in Novec-649 up to 50GHz, with TRL calibration performed in air (black) and TRL calibration performed with calibration structures

Appendix C

Structural Dimension Verification

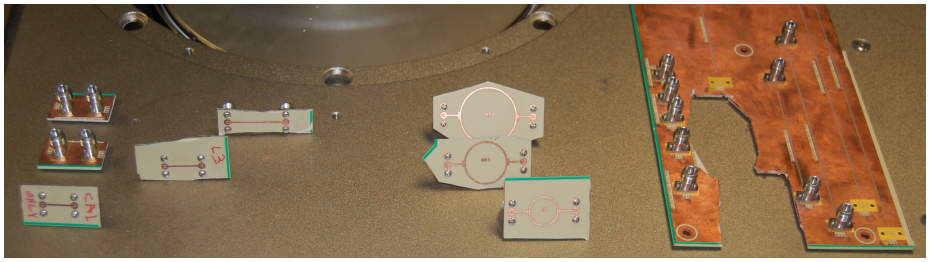

Figure C.1: Photograph of all M6 structures.

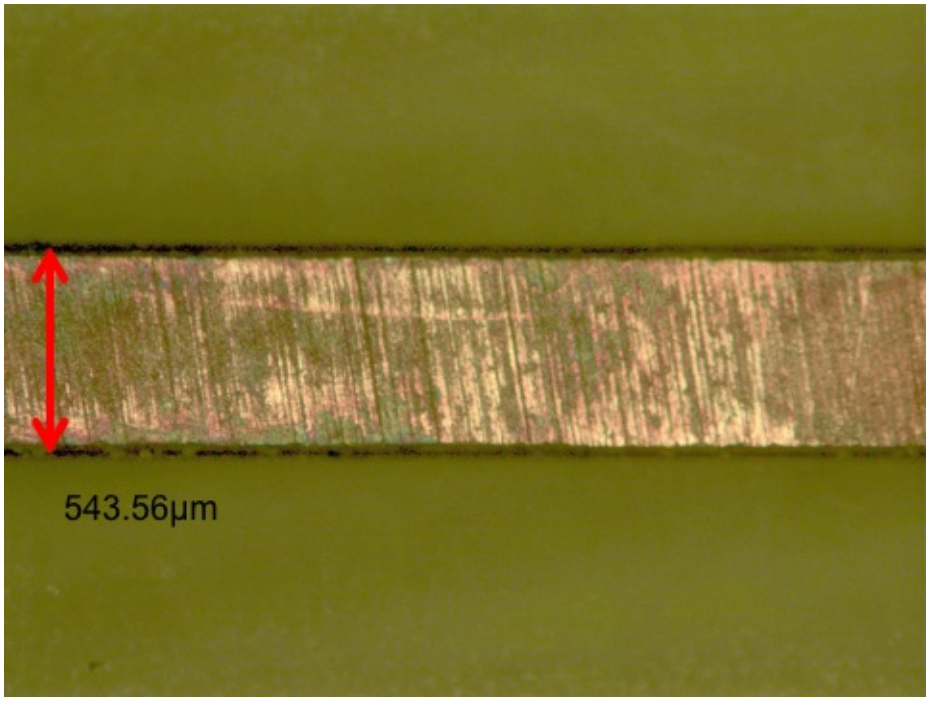

Figure C.2: Microstrip line under magnification (10x).

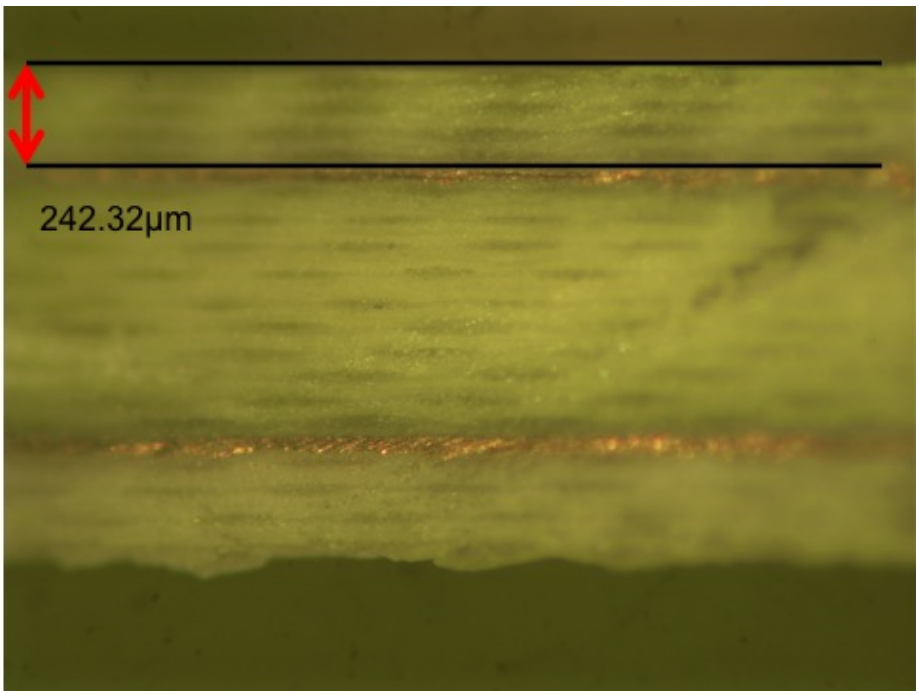

Figure C.3: Microstrip cross section under magnification (10x).

The following were produced using Alpha-Step 200 profilometer. In the case of the conductor height we can expect this instrument to produce an absolute measurement. In the case of C.5 and C.6 the reading produced by the profilometer cannot be used to provide an absolute roughness. However, by establish the peak-to-peak different of the dielectric weave, an approximation of the roughness (represented as the maximum peak-to-peak distance) can be provided. As previously mention, roughness was not factored into the simulations used in this work.

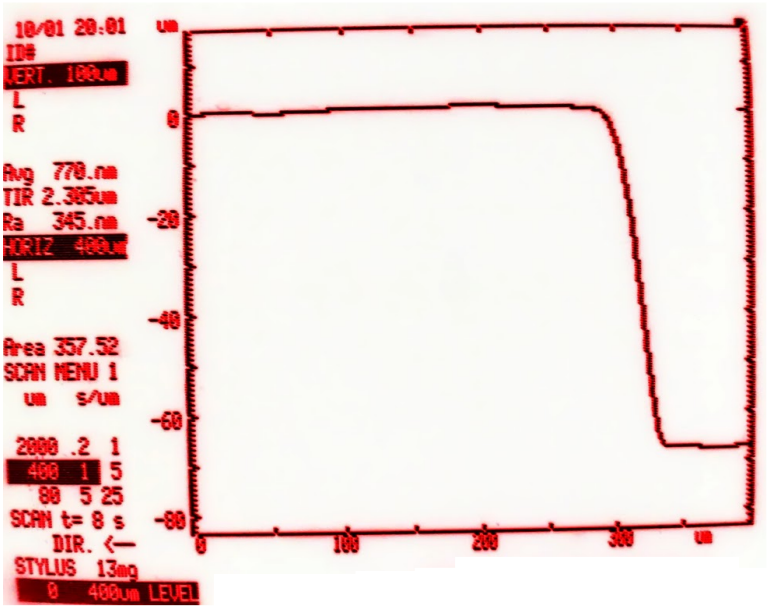

Figure C.4: Height of L2 conductor.

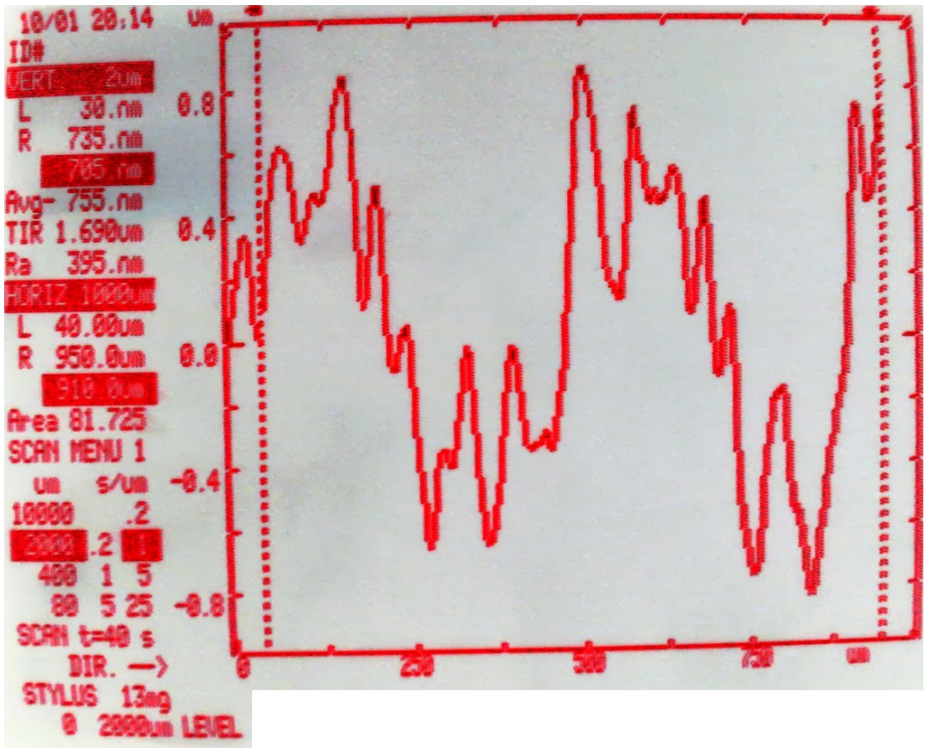

Figure C.5: Peak-to-Peak height of dielectric due to weave and resin.

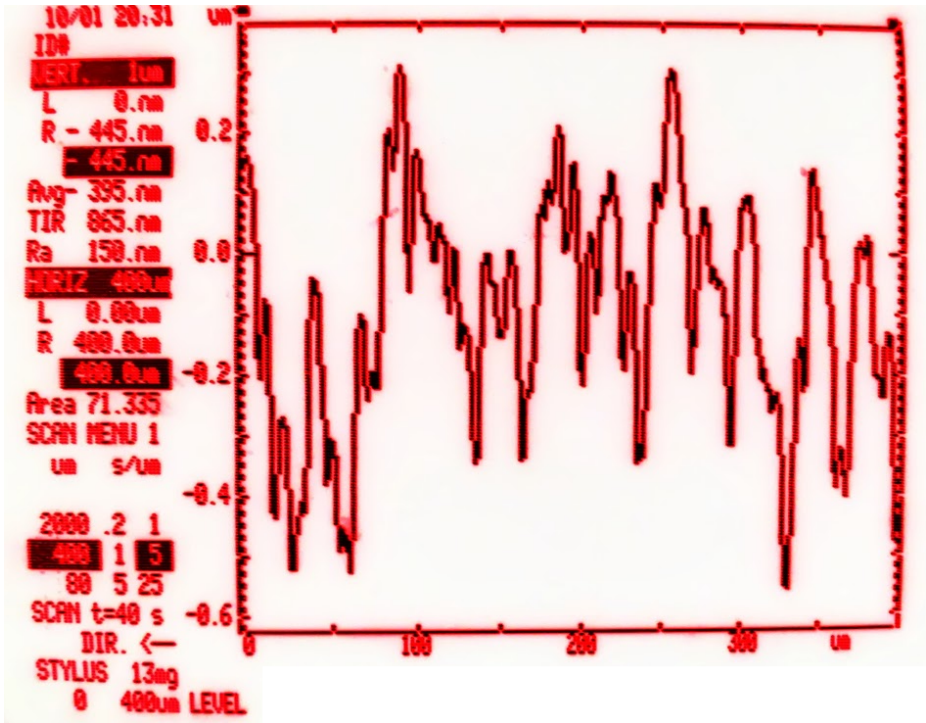

Figure C.6: Irregularity along microstrip conductor.

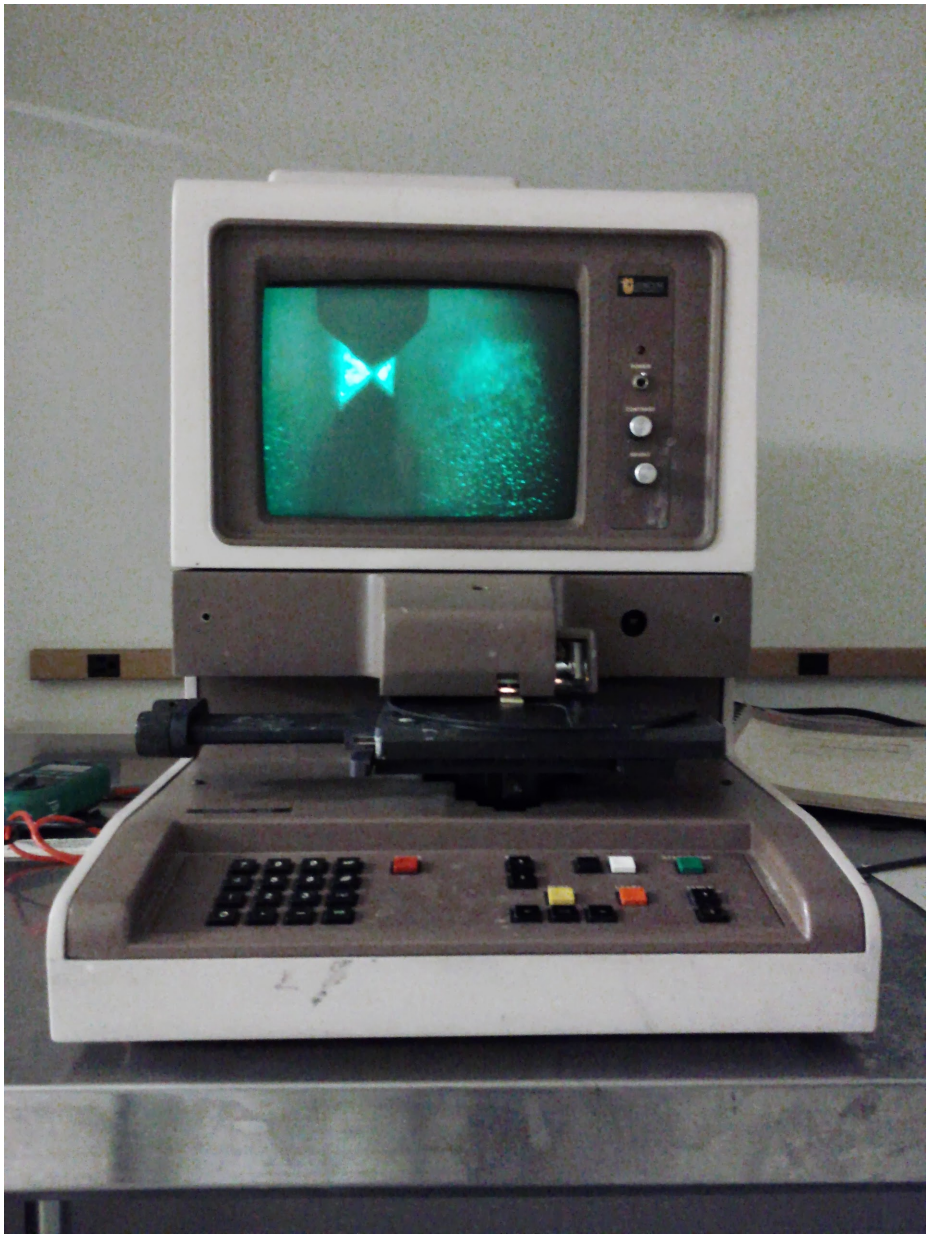

Figure C.7: Tencor Alphastep 200 Profilometer.

Appendix D

Simulation and Measurement Comparison Algorithm

To improve upon the empirical fitting of simulated insertion loss to measured insertion loss via a numerical optimization, a means of extracting the effective permittivity and Q factor (both loaded and unloaded) from a touchstone file containing scattering parameters associated with the frequency response of a ring resonator structure is required. The following MATLAB script utilizes the equations introduced in Section 2.4

```
clear all;

% Equations sourced from "Characterization of liquid crystal polymer for
% high frequency system-in-a-package applications" (DOI:
% 10.1109/TADVP.2002.807593)

% cell2str function by Per-Anders Ekstrom
% http://www.mathworks.com/matlabcentral/fileexchange/authors/25287
%19 Feb 2007 (Updated 20 Feb 2007)

% cell2num by "Darren"
% http://www.mathworks.com/matlabcentral/fileexchange/authors/28438
%14 Jun 2007 (Updated 15 Jun 2007)
```

```
14
15 colorgroup = {'k','k','r','r','b','b','g','g'};
16 stylegroup = {'d','*','d','*','d','*','d','*'};
17 leggroup={'AIR VNA','AIR HFSS','NOV VNA','NOV HFSS','FC VNA',
       'FC HFSS','HFE VNA','HFE HFSS'};
18 datagroup = {'R5_AIR_VNA_AIR_CAL_1','R5_AIR_HFSS','
       R5_NOV_VNA_NOV_Cal_1','R5_NOV_HFSS','R5_FC_VNA_FC_Cal_1','
       R5_FC_HFSS','R5_HFE_VNA_HFE_Cal_1','R5_HFE_HFSS'};
19 number_files = 6;
20
21 % Frequency Scaling in s2p file
22 scale = 1e9;
23
24 % Ring Radius (um)
25 r=8703.056*10^-6;
26
27 % Minimum height difference between peak and neighboring
       values
28 p_thres = -20;
29 % Minimum peak separation
30 p_space = 10000;
31
32 loop=0;
33 while loop<number_files
34         loop=loop+1;
35
36         % Use RF Toolbox to process s2p files
```

```
37          data_m = read(rfdata.data,strcat(cell2str(datagroup(
                loop)),'.s2p'));
38          f = data_m.Freq;
39          s_params_m = extract(data_m,'S_PARAMETERS',50);
40          s21 = db(s_params_m(2,1,:));
41          s21 = squeeze(s21); % Remove singleton dimensions, i.
                e. (:,:,N) to (N)
42
43          F_ReSamp = 0:1e5:5e10; % New underlying space
44          S21_ReSamp = interp1(f,s21,F_ReSamp,'pchip');
45
46          % find peak locations
47          [p l] = findpeaks(S21_ReSamp, 'minpeakdistance',
                p_space, 'minpeakheight', p_thres);
48
49          % Calculate Effective Permittivity
50          for i = 1:length(l)
51                  peakfreq(i) = F_ReSamp(l(i));
52                  er_eff(i) = (((i)*3e8)/(2*pi*r*F_ReSamp(l(i))
                        ))^2;
53          end
54
55          figure(1);
56          title('Effective Permittivity');
57          p1=plot(peakfreq,er_eff); hold on;
58          set(p1,'Color',cell2str(colorgroup(loop)),'Line',
                cell2str(stylegroup(loop)));
```

```
59          axis([0  50e9  2.7  3.2])
60          legend(leggroup,'Location','SouthEast');
61
62          % Calculate Q
63
64          for i = 1:length(l)
65
66              % Find S21 (dB) at the peak
67              j = l(i);
68              s21_max = S21_ReSamp(j);
69
70              % Find the lower 3dB frequency
71              while (abs(s21_max - S21_ReSamp(j)) < 2.9999999
                    && j - 1 > 0)
72                  j = j - 1;
73              end;
74              lower_3db(i) = F_ReSamp(j);
75              lower_3db_atten(i) = (S21_ReSamp(j)+S21_ReSamp(j
                    -1))/2;
76
77              X = sprintf('Attenuation (Lower) %f [%f Hz]',abs(
                    p(i)-lower_3db_atten(i)),peakfreq(i));
78              disp(X)
79
80              % reset location to the peak
81              j = l(i);
82
```

```
83              % Find the upper 3dB frequency
84              while (abs(S21_ReSamp(j) - s21_max) < 2.9999999
                    && (j + 1) < length(S21_ReSamp))
85                  j = j + 1;
86              end;
87              upper_3db(i) = F_ReSamp(j);
88              upper_3db_atten(i) = (S21_ReSamp(j)+S21_ReSamp(j
                    -1))/2;
89
90              X = sprintf('Attenuation (Upper) %f [%f Hz]',abs(
                    p(i)-upper_3db_atten(i)),peakfreq(i));
91              disp(X)
92
93              bw_3db(i) = upper_3db(i) - lower_3db(i);
94              % Loaded Q
95              Q_L(i)=(F_ReSamp(l(i))/bw_3db(i));
96              % Unloaded Q
97              Q_0(i)=(Q_L(i)/(1-db2mag(S21_ReSamp(l(i)))));
98
99          end;
100
101         figure(2);
102         title('Loaded Q (Interpolated)');
103         p1=plot(peakfreq,Q_L); hold on;
104         set(p1,'Color',cell2str(colorgroup(loop)),'Line',
                cell2str(stylegroup(loop)));
105         axis([0 50e9 0 120])
```

```
106             legend(leggroup,'Location','Southeast');
107
108             figure(3);
109             title('Unloaded Q (Interpolated)');
110             p1=plot(peakfreq,Q_0); hold on;
111             set(p1,'Color',cell2str(colorgroup(loop)),'Line',
                    cell2str(stylegroup(loop)));
112             axis([0 50e9 0 130])
113             legend(leggroup,'Location','Southeast');
114
115 end;
```

Appendix E

Extracted Dielectric Properties

The following data are provided to supplement the plots of the dielectric properties of the substrate in Air and the fluids themselves, originally provided in Figure 3.10 and Figure 3.11.

Extracted relative permittivity values (interpolated to a reduced resolution).

Freq	Air HFSS	FC HFSS	FC Probe	NOV HFSS	NOV Probe	HFE HFSS	HFE Probe
0	3.603090e+00	1.800000e+00	1.343644e+01	1.820182e+00	1.938504e+01	6.270000e+00	2.237611e+01
1000000000	3.610000e+00	1.800000e+00	1.953058e+00	1.815000e+00	2.049785e+00	6.270000e+00	7.641705e+00
2000000000	3.617188e+00	1.800000e+00	1.907300e+00	1.809609e+00	2.006300e+00	6.270000e+00	7.450800e+00
3.000000e+09	3.623611e+00	1.800000e+00	1.872552e+00	1.804792e+00	1.961856e+00	6.230000e+00	7.139931e+00
4.000000e+09	3.628229e+00	1.800000e+00	1.897884e+00	1.801328e+00	1.980443e+00	5.871617e+00	6.830975e+00
5.000000e+09	3.630000e+00	1.800000e+00	1.875600e+00	1.800000e+00	1.953700e+00	5.500059e+00	6.487100e+00
6.000000e+09	3.630000e+00	1.798688e+00	1.845122e+00	1.800000e+00	1.924914e+00	5.372032e+00	6.125230e+00
7.000000e+09	3.630000e+00	1.795264e+00	1.871511e+00	1.800000e+00	1.935759e+00	5.288188e+00	5.819690e+00
8.000000e+09	3.630000e+00	1.790496e+00	1.838700e+00	1.800000e+00	1.912200e+00	5.139808e+00	5.508800e+00
9.000000e+09	3.630000e+00	1.785152e+00	1.813367e+00	1.800000e+00	1.885537e+00	4.810961e+00	5.217830e+00
1.000000e+10	3.630000e+00	1.780000e+00	1.837926e+00	1.800000e+00	1.895881e+00	4.519579e+00	4.994674e+00
1.100000e+10	3.630000e+00	1.774576e+00	1.809400e+00	1.798347e+00	1.874500e+00	4.417146e+00	4.757100e+00
1.200000e+10	3.630000e+00	1.768288e+00	1.815522e+00	1.794240e+00	1.876052e+00	4.349956e+00	4.560622e+00
1.300000e+10	3.630000e+00	1.761712e+00	1.829561e+00	1.788960e+00	1.885373e+00	4.240178e+00	4.397507e+00
1.400000e+10	3.630000e+00	1.755424e+00	1.793300e+00	1.783787e+00	1.855000e+00	4.064571e+00	4.213300e+00
1.500000e+10	3.630000e+00	1.750000e+00	1.797928e+00	1.780000e+00	1.854496e+00	3.895433e+00	4.064889e+00
1.600000e+10	3.630000e+00	1.745212e+00	1.804826e+00	1.777680e+00	1.858744e+00	3.759727e+00	3.948885e+00
1.700000e+10	3.630000e+00	1.740596e+00	1.817700e+00	1.775840e+00	1.866700e+00	3.640305e+00	3.843400e+00
1.800000e+10	3.630000e+00	1.736374e+00	1.788813e+00	1.774160e+00	1.838192e+00	3.545601e+00	3.704119e+00
1.900000e+10	3.630000e+00	1.732768e+00	1.802550e+00	1.772320e+00	1.851260e+00	3.469630e+00	3.631621e+00
2.000000e+10	3.630000e+00	1.730000e+00	1.806500e+00	1.770000e+00	1.848400e+00	3.379709e+00	3.534300e+00
2.100000e+10	3.632080e+00	1.728143e+00	1.792926e+00	1.766330e+00	1.840033e+00	3.252200e+00	3.457611e+00
2.200000e+10	3.637040e+00	1.726692e+00	1.798941e+00	1.761389e+00	1.842267e+00	3.123870e+00	3.393863e+00
2.300000e+10	3.642960e+00	1.725000e+00	1.802500e+00	1.756284e+00	1.845300e+00	3.030081e+00	3.338500e+00
2.400000e+10	3.647920e+00	1.722500e+00	1.778150e+00	1.752119e+00	1.826489e+00	2.951247e+00	3.274478e+00
2.500000e+10	3.650000e+00	1.720000e+00	1.811445e+00	1.750000e+00	1.852845e+00	2.868464e+00	3.263424e+00
2.600000e+10	3.649369e+00	1.718253e+00	1.803600e+00	1.749423e+00	1.845300e+00	2.771442e+00	3.215500e+00
2.700000e+10	3.647706e+00	1.716747e+00	1.797467e+00	1.749060e+00	1.843533e+00	2.702302e+00	3.173141e+00
2.800000e+10	3.645358e+00	1.715000e+00	1.808959e+00	1.748787e+00	1.854029e+00	2.675157e+00	3.141033e+00
2.900000e+10	3.642674e+00	1.712558e+00	1.805800e+00	1.748476e+00	1.860000e+00	2.657440e+00	3.106700e+00
3.000000e+10	3.640000e+00	1.710000e+00	1.814118e+00	1.748000e+00	1.855200e+00	2.642395e+00	3.065732e+00
3.100000e+10	3.636273e+00	1.707835e+00	1.811319e+00	1.747146e+00	1.850974e+00	2.629665e+00	3.036007e+00
3.200000e+10	3.632025e+00	1.705814e+00	1.801900e+00	1.745304e+00	1.836500e+00	2.619042e+00	2.994300e+00
3.300000e+10	3.630000e+00	1.703876e+00	1.837024e+00	1.744515e+00	1.863233e+00	2.609642e+00	2.978333e+00
3.400000e+10	3.637500e+00	1.701959e+00	1.796655e+00	1.743142e+00	1.839199e+00	2.601937e+00	2.923837e+00
3.500000e+10	3.645000e+00	1.700000e+00	1.792900e+00	1.742000e+00	1.829600e+00	2.597055e+00	2.893900e+00
3.600000e+10	3.643440e+00	1.697893e+00	1.837566e+00	1.741079e+00	1.870904e+00	2.593734e+00	2.898607e+00
3.700000e+10	3.639720e+00	1.695680e+00	1.784585e+00	1.740230e+00	1.824630e+00	2.587822e+00	2.825881e+00
3.800000e+10	3.635280e+00	1.693520e+00	1.800800e+00	1.739441e+00	1.840900e+00	2.572652e+00	2.813400e+00
3.900000e+10	3.631560e+00	1.691573e+00	1.844489e+00	1.738701e+00	1.878315e+00	2.553024e+00	2.825974e+00
4.000000e+10	3.630000e+00	1.690000e+00	1.764748e+00	1.738000e+00	1.805949e+00	2.533489e+00	2.749300e+00
4.100000e+10	3.630000e+00	1.688907e+00	1.826100e+00	1.737369e+00	1.861400e+00	2.512243e+00	2.775000e+00
4.200000e+10	3.630000e+00	1.688120e+00	1.805174e+00	1.736810e+00	1.843478e+00	2.491333e+00	2.747548e+00
4.300000e+10	3.630000e+00	1.687380e+00	1.740975e+00	1.736267e+00	1.789862e+00	2.470667e+00	2.692569e+00
4.400000e+10	3.630000e+00	1.686427e+00	1.853400e+00	1.735682e+00	1.888500e+00	2.450000e+00	2.767200e+00
4.500000e+10	3.630000e+00	1.685000e+00	1.837615e+00	1.735000e+00	1.883549e+00	2.431004e+00	2.742054e+00
4.600000e+10	3.630000e+00	1.681840e+00	1.748863e+00	1.734192e+00	1.800756e+00	2.410641e+00	2.678678e+00
4.700000e+10	3.630000e+00	1.676220e+00	1.895700e+00	1.733276e+00	1.936300e+00	2.376243e+00	2.764400e+00
4.800000e+10	3.630000e+00	1.668680e+00	1.861159e+00	1.732264e+00	1.898511e+00	2.322487e+00	2.729474e+00
4.900000E+10	3.630000e+00	1.662558e+00	1.828941e+00	1.733681e+00	1.875300e+00	2.303024e+00	2.712588e+00
5.000000E+10	3.630000e+00	1.655680e+00	1.904489e+00	1.731319e+00	1.943024e+00	2.392730e+00	2.738678e+00

Extracted loss tangent values (interpolated to a reduced resolution).

Freq	Air HFSS	FC HFSS	FC Probe	NOV HFSS	NOV Probe	HFE HFSS	HFE Probe
0	-1.769752e-03	4.297743e-02	-7.440016e-01	2.645313e-02	-3.536155e+00	1.893194e-01	8.402083e-01
1000000000	9.000000e-05	4.000000e-02	9.370937e-03	2.500000e-02	1.527587e-02	1.800000e-01	5.446962e-02
2000000000	1.973149e-03	3.775313e-02	1.751167e-02	2.377188e-02	1.619897e-02	1.868074e-01	1.274091e-01
3.000000e+09	3.653396e-03	3.619722e-02	-1.021635e-02	2.282500e-02	1.233984e-03	2.026259e-01	1.877803e-01
4.000000e+09	4.904446e-03	3.529271e-02	-2.900298e-03	2.221562e-02	1.170562e-02	2.442460e-01	2.371308e-01
5.000000e+09	5.500000e-03	3.500000e-02	7.357646e-03	2.200000e-02	1.161898e-02	2.961330e-01	2.891122e-01
6.000000e+09	5.659120e-03	3.591149e-02	-2.340297e-02	2.231200e-02	-1.054362e-02	3.365604e-01	3.275906e-01
7.000000e+09	5.766510e-03	3.809447e-02	-9.897972e-03	2.305600e-02	-4.493709e-03	3.744078e-01	3.621079e-01
8.000000e+09	5.844340e-03	4.072170e-02	-7.940393e-03	2.394400e-02	-8.890283e-04	4.109142e-01	3.969649e-01
9.000000e+09	5.914780e-03	4.296596e-02	-4.235819e-02	2.468800e-02	-2.607626e-02	4.515832e-01	4.160792e-01
1.000000e+10	6.000000e-03	4.400000e-02	-1.634010e-02	2.500000e-02	-7.444749e-03	4.787226e-01	4.424439e-01
1.100000e+10	6.100000e-03	4.412136e-02	-2.249364e-02	2.500000e-02	-9.975994e-03	4.844704e-01	4.610792e-01
1.200000e+10	6.200000e-03	4.419624e-02	-3.854214e-02	2.500000e-02	-2.183492e-02	4.875905e-01	4.718664e-01
1.300000e+10	6.300000e-03	4.425045e-02	-3.533460e-02	2.500000e-02	-2.025179e-02	4.934769e-01	4.807962e-01
1.400000e+10	6.400000e-03	4.430977e-02	-3.786316e-02	2.500000e-02	-2.447439e-02	5.042400e-01	4.904232e-01
1.500000e+10	6.500000e-03	4.440000e-02	-3.855592e-02	2.500000e-02	-2.492093e-02	5.100000e-01	4.991157e-01
1.600000e+10	6.601778e-03	4.457714e-02	-4.163877e-02	2.521050e-02	-2.802632e-02	5.100000e-01	5.027257e-01
1.700000e+10	6.705333e-03	4.483429e-02	-4.071079e-02	2.575151e-02	-2.705309e-02	5.100000e-01	5.027059e-01
1.800000e+10	6.808000e-03	4.510286e-02	-4.272874e-02	2.648726e-02	-3.101035e-02	5.103200e-01	5.069729e-01
1.900000e+10	6.907111e-03	4.531429e-02	-6.889782e-02	2.728201e-02	-5.176251e-02	5.114815e-01	4.974789e-01
2.000000e+10	7.000000e-03	4.540000e-02	-3.952394e-02	2.800000e-02	-3.267691e-02	5.117819e-01	5.030982e-01
2.100000e+10	7.079011e-03	4.535840e-02	-5.562816e-02	2.853379e-02	-4.354481e-02	5.061200e-01	4.932062e-01
2.200000e+10	7.146365e-03	4.525920e-02	-5.787739e-02	2.908912e-02	-4.392449e-02	5.002941e-01	4.925148e-01
2.300000e+10	7.214214e-03	4.514080e-02	-5.303745e-02	3.000000e-02	-4.226955e-02	5.024166e-01	4.868354e-01
2.400000e+10	7.294709e-03	4.504160e-02	-5.385483e-02	3.400000e-02	-4.037452e-02	5.082459e-01	4.821246e-01
2.500000e+10	7.400000e-03	4.500000e-02	-6.632741e-02	3.800000e-02	-5.289800e-02	5.096625e-01	4.684286e-01
2.600000e+10	7.598292e-03	4.504160e-02	-6.548015e-02	3.905185e-02	-5.392077e-02	5.059441e-01	4.668636e-01
2.700000e+10	7.800000e-03	4.514080e-02	-6.719850e-02	3.974815e-02	-5.812958e-02	5.003578e-01	4.610352e-01
2.800000e+10	7.900000e-03	4.525920e-02	-6.075399e-02	4.000000e-02	-5.211855e-02	4.926250e-01	4.635468e-01
2.900000e+10	7.967308e-03	4.535840e-02	-6.290841e-02	4.000000e-02	-4.989247e-02	4.833600e-01	4.583964e-01
3.000000e+10	8.000000e-03	4.540000e-02	-6.833750e-02	4.000000e-02	-5.395430e-02	4.774104e-01	4.534323e-01
3.100000e+10	8.000000e-03	4.504055e-02	-5.661014e-02	4.000000e-02	-4.843665e-02	4.733759e-01	4.531309e-01
3.200000e+10	8.000000e-03	4.410565e-02	-6.698485e-02	4.000000e-02	-5.673836e-02	4.696211e-01	4.492870e-01
3.300000e+10	8.025926e-03	4.281047e-02	-7.578838e-02	4.000000e-02	-6.960239e-02	4.660120e-01	4.341567e-01
3.400000e+10	8.074074e-03	4.137020e-02	-5.009504e-02	4.000000e-02	-4.595940e-02	4.628099e-01	4.453658e-01
3.500000e+10	8.100000e-03	4.000000e-02	-8.187852e-02	4.000000e-02	-7.006996e-02	4.597980e-01	4.316321e-01
3.600000e+10	8.066166e-03	3.880182e-02	-6.836768e-02	3.967932e-02	-5.699890e-02	4.567594e-01	4.268183e-01
3.700000e+10	7.987888e-03	3.756828e-02	-6.126114e-02	3.887796e-02	-5.830795e-02	4.534772e-01	4.278476e-01
3.800000e+10	7.900000e-03	3.605061e-02	-8.396268e-02	3.783694e-02	-7.034603e-02	4.497345e-01	4.157603e-01
3.900000e+10	7.804730e-03	3.400000e-02	-7.466302e-02	3.679728e-02	-6.310545e-02	4.453144e-01	4.039161e-01
4.000000e+10	7.700000e-03	3.000000e-02	-7.556711e-02	3.600000e-02	-6.458566e-02	4.400000e-01	4.024468e-01
4.100000e+10	7.609043e-03	3.139627e-02	-1.007612e-01	3.553671e-02	-8.971742e-02	4.321644e-01	3.787027e-01
4.200000e+10	7.527130e-03	3.474880e-02	-8.658995e-02	3.500000e-02	-8.110277e-02	4.210405e-01	3.780539e-01
4.300000e+10	7.440696e-03	3.880320e-02	-1.003461e-01	3.337367e-02	-9.610082e-02	4.077015e-01	3.685869e-01
4.400000e+10	7.336174e-03	4.230507e-02	-1.025683e-01	3.113128e-02	-9.229547e-02	3.932204e-01	3.526670e-01
4.500000e+10	7.200000e-03	4.400000e-02	-9.853865e-02	3.000000e-02	-9.268495e-02	3.786703e-01	3.461145e-01
4.600000e+10	6.940580e-03	4.434293e-02	-1.083384e-01	3.458333e-02	-9.670504e-02	3.651242e-01	3.508071e-01
4.700000e+10	6.585507e-03	4.462080e-02	-9.579575e-02	4.000000e-02	-9.213448e-02	3.532530e-01	3.391694e-01
4.800000e+10	6.300000e-03	4.482720e-02	-8.938930e-02	4.091667e-02	-8.197755e-02	3.418911e-01	3.362664e-01
4.900000e+10	6.125271e-03	4.500565e-02	-1.046703e-01	4.209166e-02	-9.281344e-02	3.310000e-01	3.325683e-01
5.000000e+10	6.000001e-03	4.500000e-02	-5.905386e-02	5.075833e-02	-4.780277e-02	3.211102e-01	3.440071e-01